

國立台灣大學理學院大氣科學系

博士論文

Department of Atmospheric Sciences

College of Science

National Taiwan University

Doctoral Dissertation



人為氣膠對印度夏季季風自肇始前至消退之影響

Effects of anthropogenic aerosols on the Indian Summer

Monsoon from pre-onset to withdrawal

黃冠慈

Kuan-Tzu Huang

指導教授： 隋中興 博士

Advisor: Chung-Hsiung Sui Ph.D.

中華民國 113 年 2 月

February 2024

國立臺灣大學博士學位論文 口試委員會審定書

本論文係 黃冠慈 君 (學號 D04229004) 在國立臺灣大學大氣科學學系、所完成之博士學位論文，於民國 113 年 1 月 24 日承下列考試委員審查通過及口試及格，特此證明

口試委員：

隋中興

(簽名)

(指導教授)

潘志明

陳維婷

羅淑娟

劉清煌

陳正平

張瓊文

游政宏

(簽名)

系主任、所長

致謝

歷經多時終於讓研究有一個階段性的結果並完成這本論文，非常感謝過程中多位師長的幫助。在此研究告一個段落之際，我想將感謝之意向諸位老師表達；陳正平教授、陳維婷教授、盧孟明教授及張瓊文教授。另外特別感謝羅敏輝教授、林和教授以及我的指導教授隋中興教授，三位老師在我研究遭逢困頓及健康狀況低潮時給予諸多的鼓勵、指導和幫助，也富有耐心地不斷和我討論並解決研究上的問題。同時也感謝系主任游政谷、林博雄老師、徐光榮老師及吳明進老師提供助教及系上工作職務讓我免於收入匱乏的煩惱。這本論文得以完成最大的感謝要獻給我的父母，感謝他們的支持並且願意去理解作為博士生可能遇到的問題和挑戰，施予耐心與陪伴。感謝那些在這段過程中參與我的生命但可惜沒能一起走到終點的人，既是曾經重要的支持，如今亦是我成長的根源。最後我想將這本論文及研究成果獻給天上的阿公阿嬤，有他們的人生智慧以及曾經努力打下的基礎，才能使我得以堅持走完這條道路。

中文摘要

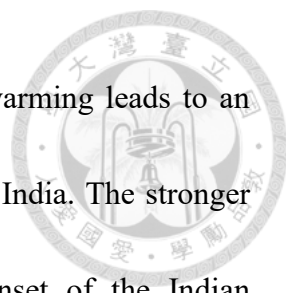
本研究使用國家大氣研究中心(NCAR)社區地球系統模式來研究人為氣膠對印度夏季季風的影響。研究中設計兩組實驗皆以氣候年循環海溫為模式下邊界條件進行 30 年模擬，實驗組(AERO)以 2000 年氣候平均人為氣膠排放資料驅動印度地區人為氣膠排放，控制組(CTL)則以 1850 年氣候平均人為氣膠排放資料驅動，實驗中僅考慮氣膠直接效應。實驗結果顯示在 AERO 中的印度夏季季風集合平均肇始日與 CTL 相似，各年的肇始日機率分佈相比 CTL 分佈更廣。與 CTL 相比，AERO 中印度夏季季風於初春肇始期間環流轉變較急遽，而於初秋減退期間轉變較平緩。印度夏季季風肇始前，氣膠驅使的環流變化特徵於東北印度半島上空顯示上升運動以及阿拉伯海上空反旋式環流加強。阿拉伯海上空增強之反旋式環流導致季風肇始前增加 16%自然源沙塵自中亞地區傳送至北印度地區。季風肇始前境外沙塵沿反氣旋環流由境外移入印度半島加上人為排放氣膠在青藏高原南側累積的輻射加熱(elevated heat pump)效應與半島上的氣膠黯化(aerosol dimming)效應影響區域氣候：高原南側氣流受輻射加熱上升；印度半島上氣膠吸收輻射增溫大氣冷卻地面，使得大氣受到氣膠輻射加熱導致海陸溫差加大產生氣旋式上升運動。前述氣膠-輻射-環流的交互作用越強則印度夏季季風肇始日期越早發生。在夏季季風期間，氣膠因降雨洗除作用及季節環流改變(南風分量增加)而使濃度降低且向北延伸，導致高原輻射加熱效應局限於西北印度地區且半島上氣膠黯淡效應減弱季風氣旋環流與降水(氣膠增加低層大氣穩定度、中高層大氣氣膠輻射改變海陸溫差效應不明顯)。夏季季風消退期間類似的氣膠黯淡效應持續作用，使得印度半島東側跟孟加拉灣產生南(0° - 10° N)-北(10° - 25° N)氣旋-反氣旋距平，此情況與印度夏季季風於九月消退時之環流特徵相似有利於季風消退提前。

關鍵詞：印度區域氣候變化、印度夏季季風、人為氣膠、氣膠輻射驅力、自然源氣膠分布

Abstract



The NCAR Community Earth System Model is used to study the influences of anthropogenic aerosols on the Indian summer monsoon (ISM). We perform two sets of 30-year simulations subject to the prescribed perpetual SST annual cycle. One is triggered by the year 2000 climatology anthropogenic aerosol emissions data over the Indian Peninsula (referred to as AERO), and the other one is by the year 1850 (referred to as CTL). Only aerosol direct effects are included in the experiments. In our results, the transition of ISM in AERO relative to the CTL exhibits a similar ensemble-mean onset date with a larger spread, and more abrupt onset in late spring, and an earlier but more gradual withdrawal in early fall. The aerosols-induced circulation changes feature an upward motion over the northeastern Indian Peninsula and strengthened anticyclonic circulation over the Arabia Sea in the pre-monsoon season, and a northward shift of monsoon flow in the developed monsoon period along with strengthened local meridional circulation over northern India. The strengthened anticyclonic circulation over Arabia Sea caused a 16% increase in natural dust transport from the Middle East in the pre-monsoon season. In the pre-monsoon period, dust transported along anticyclonic circulation into India and the accumulation of anthropogenic aerosols influence regional climate by elevated heat pump over the Tibet and the aerosol dimming effect over India Peninsula. The elevated aerosol heating induces ascending motion over the southern Tibetan area,



while aerosol dimming-induced surface cooling and atmospheric warming leads to an increased land-sea temperature difference and cyclonic ascent over India. The stronger aerosols-radiation-circulation interaction corresponds to earlier onset of the Indian Summer Monsoon. During the developed monsoon period, aerosol concentrations decrease due to rainfall washout effects and shift northward by southwesterly monsoon flow. As a result, the radiative heating effect on the plateau is limited to the northwestern region of India, and the dimming effect over the peninsula weakens cyclonic monsoon circulation and precipitation due to the increased atmospheric stability and insignificant land-sea temperature difference. During the monsoon withdrawal, similar aerosol dimming effect results in a dipole pattern of south (0° - 10° N) to north (10° - 25° N) cyclonic-anticyclonic anomalies in Eastern Indian Peninsula and the Bay of Bengal. The above aerosol induced circulation change resembles the tendency change of flow in September, favoring early monsoon withdrawal.

Keywords: Indian local climate change, Indian Summer Monsoon, anthropogenic aerosols, aerosol radiative forcing, natural dust distribution



Table of Contents

國立台灣大學博士學位論文口試委員會審定書	i
致謝	ii
中文摘要	iii
Abstract.....	iv
Table of Contents.....	vi
List of Tables	viii
List of Figures.....	ix
Chapter 1 Introduction.....	1
Chapter 2 Model and experiment designs	8
2.1 Model.....	8
2.2 Experiment designs	9
Chapter 3 Simulated and observed climate of ISM.....	12
3.1 Climatological evolution over India Peninsula	12
3.2 Evolution of ISM.....	13
Chapter 4 Effect of anthropogenic aerosols on Indian Summer Monsoon.....	19
4.1 Effect of anthropogenic aerosols on pre-monsoon climate	19
4.2 Effect of anthropogenic aerosols on developed monsoon climate	23
4.3 Moisture budget analysis in the developed monsoon period.....	26



4.4 Effect of anthropogenic aerosols on monsoon withdrawal and post-monsoon
climate 28

Chapter 5 Circulation changed influence on natural dust distribution in monsoon
evolution 31

Chapter 6 Discussion 34

 6.1 Comparison of the EHP and dimming effect over India 34

 6.2 The larger variability of onset date in AERO 36

Chapter 7 Summary 38

Reference 42



List of Tables

Table 1 Schemes in CESM	51
Table 2 Emission of anthropogenic aerosols (BC, OC, Sulfate) averaged within Indian region (70°-90°E, 5°-35°N) with Year 2000 data and percentage of emission differences.	52
Table 3 Ensemble-mean AOD, surface temperature, and surface energy fluxes averaged within Indian region (70°-90°E, 5°-35°N) and pre-monsoon season for AERO and AERO-CTL.	53
Table 4 Concentration differences of each aerosol species; BC, OC, Sulfate and dust in atmosphere averaged within Indian region (70°-90°E, 5°-35°N) with percentage of differences.	54
Table 5 AOD differences of dust and anthropogenic (Anthro) aerosols averaged within Indian region (70°-90°E, 5°-35°N) and northern India (70°-90°E, 20°-35°N) with percentage of differences.....	55
Table 6 Ensemble mean 850hPa atmospheric temperature and surface temperature in AERO, and temperature differences between Land(70°-90°E, 10°-20°N) and Sea (70°-90°E, 0°-10°N).	56



List of Figures

Figure 1 Emission of anthropogenic aerosols (BC, OC, and sulfate) of Year 2000 (shaded, $10^{-1} \cdot \text{Mg} \cdot \text{m}^{-2} \cdot \text{month}^{-1}$) from the IPCC AR5 emission data set (Lamarque et al. 2010a).

The sources of emission include industrial, domestic and agriculture activities.

Surface topography is superimposed in contour at 200m interval and selected

contours highlighted as following: 200m (blue dash), 600m (red dash), 1000m,

2000m, 3000m and 4000m (thick solid). The Tibetan Plateau is denoted by areas

with elevation above 4000m and shaded grey. 57

Figure 2 Time series of mean anthropogenic aerosols (BC, OC, sulfate) emission ($\text{Mg} \cdot \text{m}^{-2} \cdot \text{month}^{-1}$) of Year 2000 (*blue dash*), and the simulated annual cycle of anthropogenic aerosol optical depth (AOD, blue solid) in the Indian sub-continent region, and the differences of aerosol emission (*red dash*) and AOD (*red solid*) between Year 2000 and Year 1850, and dust AOD (*grey line*) of Year 1850. 58

Figure 3 Time-latitude distribution of climatological fields over India longitude sector (70° 90°E) (a) 500 hPa temperature, (b) surface air temperature, (c) 850 hPa zonal wind, and (d) precipitation, derived from ERA-interim and GPCP for 1979-2020. The model simulated climatological fields for the corresponding fields are shown in (e, f, g, h) derived from 25 years of AERO outputs. 59

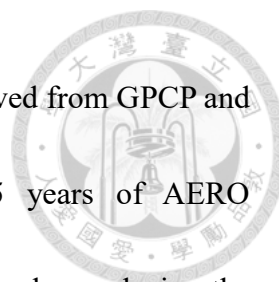
Figure 4 Climatological evolution of the zonal wind index as defined in Wang et al. (2001)



(blue line), all-India precipitation (mm, solid line), and Kerala precipitation (mm, dash line, used by India Meteorological Department to define monsoon onset) for (a) CTL, (b) AERO and (c) ERA-interim/GPCP. The standard deviation of the simulated zonal wind index of the 25 years simulations from CTL and AERO are shown in (a) (b) by blue shadings. The 25-year mean zonal wind index changes sign from negative to positive on May 12 in both CTL and AERO (monsoon onset), and from positive to negative on Oct. 20 in CTL and Oct. 10 in AERO (monsoon withdrawal). The onset and withdrawal dates are marked by vertical dashed lines, and the transition periods are shaded orange within 2 pentads before and after the mean monsoon onset and withdrawal dates. Total monsoon precipitation is 571 mm in CTL and 539 mm in AERO. 60

Figure 5 Frequency distributions of India monsoon onset and withdrawal dates (a, c) and their corresponding rate of changes (b, d) of the 25 ensemble years in CTL and AERO. The statistics is shown in box plots drawn from the first quartile (bottom) to the third quartile (top) and a horizontal line through the box at the median with the mean value marked by a cross and the date of 90% and 10% ranking marked by the sign “-” linked to the box by vertical lines. 62

Figure 6 Observed climatological fields of precipitation (mm day⁻¹, *shaded*), horizontal winds at 850 hPa (m · s⁻¹, *vector*) and geopotential height at 500 hPa (m, *red dash*)



in (a) pre-monsoon, (b) post-monsoon, and (c) withdrawal, derived from GPCP and ERA-interim. The simulated ensemble mean fields of 25 years of AERO corresponding to (a, b, c) are shown in (d, e, f). The two rectangles enclosing the area (40°-80°E, 5°-15°N) and (70°-90°E, 20°-30°N) are used to define the zonal wind index [U850(1)– U850(2)] for the evolution of ISM. 63

Figure 7 Observed climatological fields of dust AOD (shaded), horizontal winds at 850 hPa ($m \cdot s^{-1}$, vector) in (a) pre-monsoon, (b) post-monsoon, and (c) withdrawal, derived from MERRA2 and ERA-interim. The simulated ensemble mean fields of 25 years of AERO corresponding to (a, b, c) are shown in (d, e, f). 64

Figure 8 Ensemble mean fields in pre-monsoon period of AERO (March 1 to April 10) (a) vertical velocity, $-\omega$ (shaded) and horizontal wind ($m \cdot s^{-1}$, vector) at 850 hPa, (b) $-\omega$ and horizontal wind at 500 hPa, (c) 70-90°E averaged $-\omega$, (d, e, f) AERO-CTL differences corresponding to the fields shown in a, b, c. Differences of $-\omega$ are shown by contours ($-\omega < 0$ with dashed line, > 0 with thick solid line) with interval 0.04. A confidence level greater than 90% (shaded) use the Student's t-test. 65

Figure 9 Ensemble mean aerosol optical depth (AOD, shaded) and horizontal wind at 850 hPa ($m \cdot s^{-1}$, vector) in pre-monsoon period of AERO (March 1 to April 10). The AOD differences (AERO – CTL) > 0 are shown by red contours with contour interval 0.02 begin from 0. 66

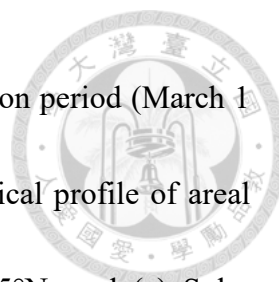


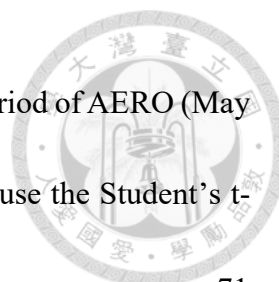
Figure 10 Ensemble mean differences (AERO – CTL) in pre-monsoon period (March 1 to April 10) (a) Surface temperature ($^{\circ}\text{C}$, *shaded*), (b) The vertical profile of areal mean temperature anomalies ($^{\circ}\text{C}$) shows in $75^{\circ}\text{-}90^{\circ}\text{E}$, $15^{\circ}\text{-}25^{\circ}\text{N}$, and (c) Solar heating rate ($^{\circ}\text{C day}^{-1}$, *shaded*) and anthropogenic aerosols concentration (mg m^{-3} , *contours at interval 0.2*). A confidence level greater than 90% (*shaded*) use the Student's t-test. 67

Figure 11 Correlation of 500 hPa TP ascending motion with (a) onset date and (b) ISM change rate over the pre-monsoon season (March 1 to April 10) in AERO (red dots) and CTL (blue dots). The correlation coefficient of TP ascending motion with onset date is -0.71 (-0.8) in AERO (CTL) and with change rate is 0.69 (0.78) in AERO (CTL). 68

Figure 12 Ensemble mean aerosol optical depth (AOD, *shaded*) and horizontal wind at 850 hPa (m s^{-1} , *vector*) in developed monsoon period of AERO (May 26 to August 3). The AOD differences (AERO – CTL) > 0 are shown by *red contours* with contour interval 0.02 begin from 0. 69

Figure 13 Ensemble mean fields in developed monsoon period of AERO (May 26 to August 3) (a) $-\omega$ (*shaded*) and horizontal wind (m s^{-1} , *vector*) at 850 hPa, (b) $-\omega$ and horizontal wind at 500 hPa, (c) $70^{\circ}\text{-}90^{\circ}\text{E}$ averaged $-\omega$ 70

Figure 14 Ensemble mean differences (AERO – CTL) of surface temperature ($^{\circ}\text{C}$, *shaded*),

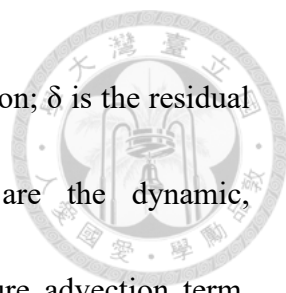


and 850 hPa circulation ($\text{m}\cdot\text{s}^{-1}$, vector) in developed monsoon period of AERO (May 26 to August 3). A confidence level greater than 90% (shaded) use the Student's t-test..... 71

Figure 15 Ensemble mean differences fields (AERO-CTL) during developed monsoon period (May 26 to August 3) of $-\omega$ are shown by contours ($-\omega < 0$ with dashed line, > 0 with thick solid line) with interval 0.04 and horizontal wind ($\text{m}\cdot\text{s}^{-1}$, vector) at (a) 850 hPa, and (b) 500 hPa, (c) 70° - 90°E averaged $-\omega$. A confidence level greater than 90% (shaded) use the Student's t-test. (d) The differences of precipitation (mm) are shown by shaded with 850-hPa horizontal winds ($\text{m}\cdot\text{s}^{-1}$, vector). (e) The vertical profile of areal mean temperature anomalies ($^\circ\text{C}$) shows in 75° - 90°E , 15° - 25°N , and (f) the solar heating rate anomalies ($^\circ\text{C}\cdot\text{day}^{-1}$, shaded) are shown with anthropogenic aerosols concentration anomalies ($\text{mg}\cdot\text{m}^{-3}$, contour); each contour is $0.2\text{mg}\cdot\text{m}^{-3}$. 72

Figure 16 Ensemble mean differences fields (AERO-CTL) during developed monsoon period (May 26 to August 3) of $-\omega$ are shown by contours ($-\omega < 0$ with dashed line, > 0 with thick solid line) with interval 0.04 in 75° - 85°E and 85° - 95°E averaged $-\omega$. A confidence level greater than 90% (shaded) use the Student's t-test. 73

Figure 17 Ensemble mean in AERO and differences for moisture budget components averaged over the SI(10° - 20°N , 70° - 90°E), WTP(25° - 35°N , 75° - 85°E), ETP(25° - 35°N , 85° - 95°E). P is precipitation; E is evaporation; $-\langle Vh \cdot \nabla hq \rangle$ is the horizontal



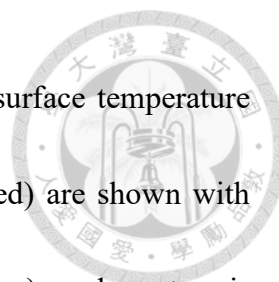
moisture advection; $-\langle\omega\partial pq\rangle$ is the vertical moisture advection; δ is the residual term; $-\langle\omega\partial pq\rangle^{\prime}$, $-\langle\omega^{\prime}\partial pq\rangle$ and $-\langle\omega^{\prime}\partial pq^{\prime}\rangle$ are the dynamic, thermodynamic, and nonlinear components of vertical moisture advection term, respectively. The terms with $^{\prime}$ means difference..... 74

Figure 18 Ensemble mean differences of moisture divergence ($\text{kg m}^{-2} \text{ s}^{-1}$) at 500 hPa in developed monsoon period (May 26 to August 3) over the Southern edge of TP.. 75

Figure 19 Aerosol optical depth (AOD, *shaded*) and 850 hPa horizontal circulation (m s^{-1} , *vector*) in withdrawal period (September 23 to October 27) of AERO. The Phase-1 and the Phase+1 represent the two weeks before and after the withdrawal date of ensemble-mean fields. *Red contour* means AOD anomalies (AERO – CTL) > 0, each contour is 0.02. 76

Figure 20 Precipitation (mm, *shaded*) and 850-hPa horizontal winds (m s^{-1} , *vector*) averaged in (a) CTL Phase-1 (Oct. 3 to Oct. 18), (b) CTL Phase+1 (Oct. 22 to Nov. 6), (c) AERO Phase-1 (Sep. 23 to Oct. 8), and (d) AERO Phase+1 (Oct. 12 to Oct. 27). *Black dash line* equals to 2 mm, and *red dash line* equals to 9 mm..... 77

Figure 21 Ensemble mean differences fields (AERO-CTL) during withdrawal period (September 23 to November 6) of $-\omega$ are shown by contours ($-\omega < 0$ with dashed line, > 0 with thick solid line) with interval 0.04 and horizontal wind (m s^{-1} , *vector*) at (a) 850 hPa, and (b) 500 hPa, (c) 70°-90°E averaged $-\omega$. A confidence level greater than



90% (shaded) use the Student's t-test. (d) The differences of surface temperature (°C), and (e) the solar heating rate anomalies (°C day⁻¹, shaded) are shown with anthropogenic aerosols concentration anomalies (mg m⁻³, *contour*); each contour is 0.2 mg m⁻³..... 78

Figure 22 Difference fields of precipitation (mm, shaded) and 850-hPa horizontal winds for (a) Phase+1 minus Phase-1 in AERO, and (b) withdrawal (Phase-1 to Phase+1) differences (AERO minus CTL)..... 79

Figure 23 Differences of dust AOD (*contour*, Δ<0 with dashed line, Δ>0 with thick solid line) and 850-hPa horizontal winds (m s⁻¹, *vector*) averaged in (a) pre-monsoon (March 1 to April 10), (b) developed monsoon (May 26 to August 3), (c) withdrawal Phase-1 (Sep. 23 to Oct. 8), and (d) AERO Phase+1 (Oct. 12 to Oct. 27). The Contour plot with interval 0.02, and significant ΔAOD with a confidence level greater than 90% using the Student's t-test. 80

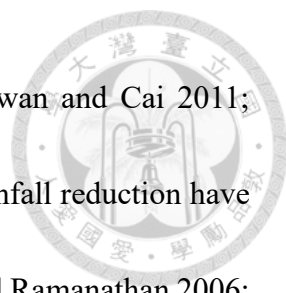
Figure 24 Correlation of 500 hPa TP ascending motion with 850-500hPa Northern Indian (25°-35°N, 70°-90°E) averaged dust (orange dots) and anthropogenic aerosol (black dots) concentration over the pre-monsoon season (March 1 to April 10) in AERO. The correlation coefficient of TP ascending motion with dust is -0.49 and anthropogenic aerosol is 0.77 in AERO. 81

Chapter 1 Introduction



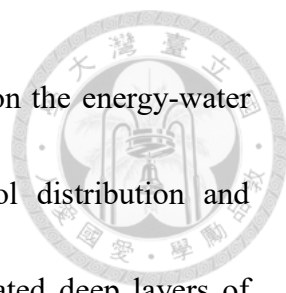
Atmospheric aerosols, which are fine particles suspended in the air, comprise a mixture of mainly sulfates, nitrates, carbonaceous (organic and black carbon) particles, sea salt, and mineral dust. Atmospheric aerosols have a strong impact on the Earth's radiation budget and climate (Stocker et al. 2014). Aerosols interact with climate system through scattering and absorption of radiation (direct effect) and through modification of the microphysical properties of clouds (indirect effect). Absorbing aerosols, such as black carbon (BC), organic carbon (OC) and dust, can both absorb and reflect sunlight, thus heating the lower-troposphere and cooling the surface. In contrast, non-absorbing aerosols, such as sulfate, generate mainly surface cooling but weak atmospheric heating. In recent decades, the BC emissions are particularly large in China and India due to energy combustion and biomass burning and have brought the world's attention (Ramanathan and Carmichael 2008; Yang et al. 2022; Wei et al. 2022).

Extensive studies concerning the roles of aerosols in the Earth's climate did not begin until the 1990s. Aerosols can affect monsoon rainfall, and regional climate change through radiative forcing and microphysical effects (Rosenfeld 2000; Li 2004; Nakajima et al. 2007; Li et al. 2007a, 2011a, 2011b; Huang et al. 2014; Guo et al. 2016). Many general circulation model (GCM) studies have investigated the impacts of aerosols on global and regional changes in precipitation (Menon et al. 2002; Lau et al. 2008; B. Wang




et al. 2009; C. Wang et al. 2009; Bollasina et al. 2011, 2013; Cowan and Cai 2011; Ganguly et al. 2012). The weakening of monsoon circulation and rainfall reduction have been attributed to aerosol effects (Ramanathan et al. 2005; Chung and Ramanathan 2006; Ramanathan and Carmichael 2008; Liu et al. 2009; Cowan and Cai 2011; Bollasina et al. 2011; Salzman et al. 2014; Krishnan et al. 2016) and equatorial Indian Ocean warming due to increased GHG (Ramanathan et al. 2005; Chung and Ramanathan 2006; Annamalai et al. 2013; Lee and Wang 2014; Sabeerali and Ajayamohan 2017).

As an integral component of the Earth's hydrological cycle, the Indian Summer Monsoon (ISM) is the largest monsoon system critical for the well-being of over two-thirds of the world's population. The observational evidence of ISM circulation experienced a significant declining trend from the 1950s together with a weakening local meridional circulation and notable precipitation decreases over north-central India and the west coast that are associated with a reduced meridional temperature gradient (Ramanathan et al. 2001b, 2005; Krishnan et al. 2013; Goyal 2014; Roxy et al. 2015; Praveen et al. 2020). Although it could potentially be altered by multidecadal variations (Shi et al. 2018) arising from internal modes of climate variability such as the Atlantic multidecadal variation (AMV) and the interdecadal Pacific oscillation (IPO) (Krishnan and Sugi 2003; Ding et al. 2008, 2009; Zhou et al. 2008; Cheng and Zhou 2014; Salzman and Cherian 2015; Jiang and Zhou 2019), the high aerosol emissions in South Asia has



made the role of aerosol effect a critical issue. The aerosol effects on the energy-water cycle and monsoon dynamics are strongly dependent on aerosol distribution and characteristics as well as its spatial and temporal variations. Elevated deep layers of radiation-absorbing aerosols can potentially affect the water cycle by significantly altering the energy balance (Ramanathan et al. 2005; Lau and Kim 2006; Lau et al. 2006).

The increase of aerosols and associated impact on the ISM has been documented in many modeling studies (e.g., Ramanathan 2005; Lau et al. 2006; Meehl et al. 2008; Ganguly et al. 2012; Bollasina et al. 2013). Ramanathan et al. (2005) used a coupled ocean-atmosphere model to show that absorbing aerosols over India could decrease monsoon precipitation by reducing surface shortwave radiation, which limits the amount of evaporation, as well as increasing atmosphere heating, which stabilizes the low-troposphere over South Asia. The high aerosol regions of the northern portion of the Indian Peninsula and the Arabian Sea are cooled relative to the oceans to the south, leading to a reduction of the meridional thermal gradient and a slowing down of the local meridional circulation. The slower circulation reduces surface evaporation and provides a positive feedback, further weakening the monsoon. In a somewhat different modeling approach, Lau et al. (2006) used an atmospheric model together with an observational analysis of Lau and Kim (2006) to emphasize the importance of temporal and regional distributions of both natural and anthropogenic aerosols not only as a forcing agent but

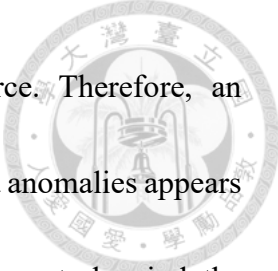


also as an integral part of a dynamical feedback mechanism involving clouds, rainfall, and winds that can alter the evolution of ISM system. They proposed the elevated heat pump (EHP) theory which posits that atmospheric heating by deep layers of BC and dust accumulated over the Indo-Gangetic Plain (IGP) and the Tibetan Plateau (TP) can induce a moisture convergence feedback, leading to increased precipitation in northern India during March to June. Specifically, the accumulation of BC and dust over the northern and southern slopes of TP absorbs shortwave over the longitudes of the Indian Peninsula during pre-monsoon periods and heats the lower and middle troposphere around the TP. The heated air rises via dry convection, creating a positive temperature anomaly in the mid-level to upper troposphere over the southern slope of TP relative to the region to the south. The rising hot air forced by the increased heating in the upper troposphere from the North Indian Ocean draws in more warm and moist air over Indian Peninsula, setting the stage for the onset of the ISM.

In our recent study (Chen et al. 2018), the anthropogenic aerosols lead to surface cooling through the decrease in surface short wave flux from October to December. The surface cooling region extends downwind of major emission source areas to western and northern India, as the aerosols are transported by the prevailing winds. The precipitation strongly reduces during October to December over western and northern India, and the reduction is mainly contributed by the vertical convergence term that is associated with

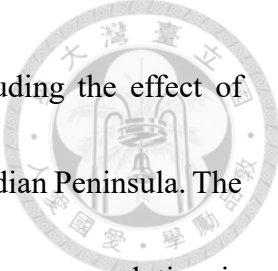
changed vertical motion by anthropogenic aerosols. Furthermore, Wang et al. (2013) further demonstrated that absorbing aerosols were particularly important in influencing the circulation and precipitation over the northern Indian regions in winter.

Similar to the radiation effect of BC and OC, the natural dust also absorbs solar radiation that causes atmospheric heating and surface cooling. Long-range transport of dust aerosols originated in the Middle East is known to be a significant source of aerosol over the Arabian Sea and Indian region during the pre-monsoon season. As a result, enhanced aerosol loading in Indian Peninsula during the pre-monsoon season is likely contributed by both anthropogenic and natural aerosols (Satheesh and Srinivasanan 2002; Badarinath et al. 2010). A recent study by Wei et al. (2022) reveals a decreasing dust transport by altered monsoon flow caused by reduced BC burden over the northern (70° - 88° E, 25° - 35° N) but increased BC burden over southern (70° - 88° E, 15° - 25° N) India during the lockdown of COVID-19. Their results indicate that the solar heating in April and May is decreased by BC reduction in northern India and the surface albedo of the TP southern slope is increased due to the reduced BC snow-darkening effect. The northern Indian atmosphere responds to this cooling with a descending motion and enhanced atmospheric stability. Furthermore, the surface and near-surface cooling over the southern slope of TP by increased albedo lead to southward cold air advection. The cooling over northern India and warming over southern India from increased crop residue burning BC



emissions induce an anomalous southward pressure gradient force. Therefore, an anomalous northward Coriolis force as the emergence of easterly wind anomalies appears to balance the anomalous pressure gradient force. Owing to anomalous easterly wind, the eastward transport of dust from the Middle East and Sahara as well as local dust emissions in the Thar Desert are suppressed.

Despite a large number of studies, there still exists a gap in our knowledge and understanding of anthropogenic aerosols and their climate effect. Aerosol processes are still poorly observed and treated in numerical models. Here, we plan to revisit the aerosol-induced monsoon variability along with aerosol's temporal transition within the monsoon evolution. In difference from the prescribed simulates aerosol radiative forcing using simulated transport and simulated aerosol spatial distributions, we use the historical emission inventory which quantified anthropogenic and biomass emissions of climate-relevant species for the period 1850-2000 by Lamarque et al. (2010). We focus especially, on the regional anthropogenic aerosols forcing over India to identify the ISM evolution responses. The dissertation is structured as follows. A brief description of the model and experimental design is given in Chapter 2. The analyses of ISM characteristics are shown in Chapter 3, including Indian monsoon characteristics in observation data and model simulation. The changes in ISM onset/withdrawal date and rate of changes are also discussed in this chapter. Each period during Indian monsoon evolution from pre-



monsoon to monsoon withdrawal are discussed in Chapter 4, including the effect of anthropogenic aerosols on the circulation and precipitation over the Indian Peninsula. The natural dust distribution response to BC climate impacts over monsoon evolution is discussed in Chapter 5. The comparison of the EHP and dimming effect over India and the larger variability of onset date in aerosol scenario are discussed in Chapter 6. At the end of the text, a summary is given in Chapter 7. Notice that some part of our results was published in the journal of Terrestrial, Atmospheric and Oceanic Sciences (TAO).

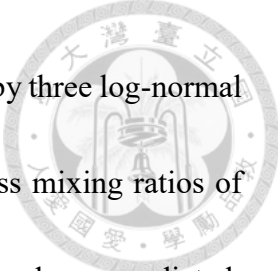


Chapter 2 Model and experiment designs

In previous studies related to monsoon circulation, global climate models are commonly used tools. Investigating the impact of aerosols on monsoon circulation involves not only assessing the model's performance in simulating monsoon circulation but also evaluating whether the model can effectively simulate aerosol effects through parameterization. Additionally, the model should provide experiments designed to regulate both direct and indirect aerosol effects. These considerations are crucial in the selection of models for this study. In Chapter 2.1, we provide an introduction to the models, while Chapter 2.2 will outline the experimental design for this research.

2.1 Model

For the current climate simulation study, we use the National Center for Atmospheric Research Community Earth System Model (CESM) v1.0.3. The atmospheric component of CESM is the Community Atmosphere Model (CAM) version 5.1 (Neale et al. 2012). CAM5.1 is the atmosphere model of the NCAR CESM1 supported by the US National Science Foundation and DOE. It has a horizontal resolution of $1.9^{\circ} \times 2.5^{\circ}$ and a vertical resolution of 30 levels from the surface to 3.6hPa with a finite volume dynamical core. Each scheme in model are list in Table 1. The properties and processes of major aerosol species included black carbon, primary organic matter, secondary organic aerosol, mineral dust, sulfate, and sea salt are treated in the three-mode modal aerosol scheme

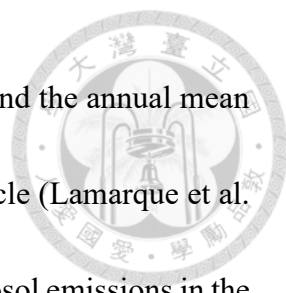


(MAM3, Liu et al. 2012). The aerosol size distribution is represented by three log-normal modes: Aitken, accumulation, and coarse modes. The associated mass mixing ratios of different aerosol components and the number concentration in each mode are predicted.

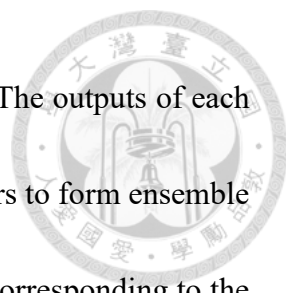
The ZM scheme (Zhang and McFarlane 1995) with dilute convective available potential energy modification is used for deep convection parameterization. The shallow convection parameterization uses the Park and Bretherton scheme (Park and Bretherton 2009). The Bretherton and Park moist turbulence scheme (Bretherton and Park 2009) is used to parameterize the stratus-radiation-turbulence interactions in boundary layer. The Morrison and Gettelman scheme (Morrison and Gettelman 2008) is used for stratiform-cloud microphysics and the mechanism of Park (2010) is used for macrophysics. The Rapid Radiation Method for GCMS (RRTMG, Iacono et al. 2008) is used for the radiative transfer calculations. The land process simulation uses the Community Land Model (CLM) version 4.0 with explicit representation of land hydrological processes and land-atmosphere interactions (Lawrence et al. 2011; Oleson et al. 2010).

2.2 Experiment designs

In this study, only the aerosol direct effect is considered by assuming concentration of aerosols to low level as cleaning environment when cloud drop activity calculated in cloud microphysics schemes. We carry out two experiments subject to the same prescribed climatological annual cycle of monthly mean sea surface temperature (SST)



and the greenhouse gas concentration at the level of the Year 1850, and the annual mean surface aerosol emissions by the Year 1850 data without seasonal cycle (Lamarque et al. 2010). The two experiments are given by different anthropogenic aerosol emissions in the India Peninsula within (70° - 95° E, 5° - 35° N) where the emission in the control simulation (CTL) is kept the same as the Year 1850 but changed to the Year 2000 in the aerosol forced experiment (AERO) that contains additional anthropogenic emissions over India Peninsula also without seasonal cycle (Lamarque et al. 2010). The emission of anthropogenic aerosols containing black carbon (BC), organic carbon (OC), and sulfate over the Indian Peninsula for the Year 2000 is shown in Fig. 1, and the value of each species are shown in Table 2. The area of highest emission resides over the IGP extending longitudinally against the Himalayan range from Bangladesh to northwestern India and Pakistan. The distribution of emission in Fig. 1 is consistent with the aerosol distribution by satellite-measured aerosol index (e.g. Bollasina et al. 2008). The emission of BC, OC and sulfate have 70%, 21% and 8% in total emission of anthropogenic aerosols as the Year 2000 data (Table 2). The areal mean aerosol emission over the Indian Peninsula for the Year 2000 and its difference from the Year 1850 are shown in Fig. 2 (dashed line). The natural aerosol i.e., dust and sea salt emissions in both simulations (CTL and AERO) are given by the Year 1850 data (Lamarque et al. 2010). And the aerosol optical depth (AOD) of natural aerosol also shows in Fig. 2 with grey line.



For the two experiments, the CESM is integrated for 30 years. The outputs of each year are considered an ensemble member, and we use the last 25 years to form ensemble averages as the annual cycle. The annual cycle of areal mean AOD corresponding to the surface emission in the India Peninsula region for the Year 2000 and its difference from the Year 1850 are shown in Fig. 2. The figure shows that the AOD of the Year 2000 increases sharply from February to April-May and then rapidly decreases in June-August following the onset of monsoon rains, and rise again mildly at the end of the rainy season in October. This is similar to the climatological annual cycle of the aerosol index over IGP based on satellite data in Bollasina et al. (2008) except the minimum AOD in AERO appears in September, one month later than that of the satellite climatology.

Chapter 3 Simulated and observed climate of ISM



3.1 Climatological evolution over India Peninsula

We first examine the model simulated climatological evolution of the ISM against the observed ISM evolution based on the 25 years of AERO outputs and the ERA-interim and GPCP data for 1979-2020. Figure 3 shows the time-latitude distributions of observed and simulated climatological fields over the Indian longitude sector (70° - 90° E) of 500-hPa temperature, surface air temperature, 850 hPa zonal wind and precipitation. Following the movement of the Sun and resultant land-sea thermal contrast, surface temperature over India starts to rise first in the central region in March ($>24^{\circ}\text{C}$) and then over the whole sub-continent in April through mid-June when the IGP reaches above 28°C . The temperature remains above 24°C from July to August and cools in September and October. The 500-hPa temperature rise in spring and summer lags that of the surface temperature rise by about one month, and falls earlier in August and September than the surface temperature does (Fig. 3a, 3b). The rapid establishment of warm temperature at 500 hPa over northern India and the Tibetan Plateau from late April and early May marks an abrupt shift of zonal wind in the lower troposphere (u_{850}) from easterly to westerly (Fig. 3c), a northward shift of the Intertropical Convergence Zone (ITCZ) and the start of monsoon rainfall over India (Fig. 3d). Likewise, the fall of 500 hPa temperature in late September and early October is associated with a reversed u_{850} change and termination

of monsoon rainfall.

The model simulated annual cycle in AERO corresponding to the observed fields is shown in Figs 3e-h. The figure shows that CESM simulates the overall evolution of ISM but overestimates rainfall in northern India to the south of the Tibetan Plateau (Fig. 3h) and the associated regional temperature (Fig. 3e) and wind (Fig. 3g) in the lower troposphere near the Tibetan Plateau. We will further evaluate the simulated circulation and rainfall in three stages of the ISM evolution below.

3.2 Evolution of ISM

Previous studies proposed different indices for describing the ISM evolution. In this study, we follow Wang et al. (2001) who defined the ISM evolution based on the difference of the 850 hPa zonal winds between a southern region of 40°-80°E, 5°-15°N and a northern region of 70°-90°E, 20°-30°N. This index is defined because low-tropospheric circulation responds to convective heating better than the upper-level circulation or vertical shear does, and the low-tropospheric vorticity is highly indicative of the strength of boundary layer moisture convergence and precipitation in regions away from the equator. In addition, such an index reflects both the intensity of the tropical westerly monsoon and the lower-tropospheric vorticity anomalies associated with the ISM trough. The ISM onset date is defined as the transition date when the circulation index changes from negative to positive values in spring. Following the same approach,

we define the ISM withdrawal date as the transition date when the index reverses from positive to negative values in fall.

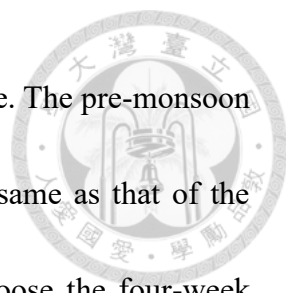


The evolution of 25-year ensemble-mean zonal wind index calculated from CTL and AERO are compared against the observed climatological index (Fig. 4). Both CTL and AERO simulate the same ensemble-mean monsoon onset date on May 12 (Fig. 4a, b) in agreement with the observed onset date (Fig. 4c). On the other hand, the mean withdrawal date in CTL is similar to the observed withdrawal date around October 20 but the withdrawal date in AERO is 10 days earlier on October 10. Besides the ensemble mean dates, we also examine the frequency distributions of ISM onset and withdrawal dates of the 25 years of simulations in Fig. 5a and 5c. Considering both ensemble mean and frequency distribution, the onset dates in AERO are not significantly different from that in CTL (Fig. 5a) but the withdrawal dates in AERO are well separated from that in CTL indicating that withdrawal occurs significantly earlier in AERO than in CTL (Fig. 5c). Note also that the onset and withdrawal dates in AERO have a larger spread than that in CTL. In addition, we define the rate of change in onset (or “onset rate” in short) and withdrawal (or “withdrawal rate”) by calculating the differences of zonal wind index within the transition periods within 2 pentads before and after the mean monsoon onset and withdrawal date (Fig. 4, orange shadings). The frequency distributions in Fig. 5b and Fig. 5d show that the onset rate in AERO is significantly larger than in CTL, but the

withdrawal rate in AERO is significantly weaker than in CTL. Possible reasons for the aerosol influences on the monsoon onset and withdrawal are discussed in Chapter 4.

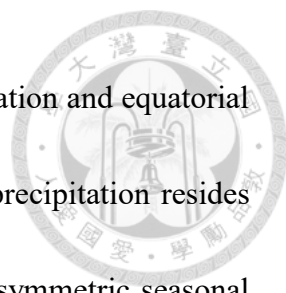
The characteristics of ISM evolution are also shown in precipitation over Indian Peninsula. India Meteorological Department defines the ISM onset by the precipitation of Kerala when it exceeds 9 mm/day. In our simulations, the ISM onset and withdrawal defined by precipitation over Kerala is consistent with the phase transition defined by the zonal wind index (Fig. 4). The climatological evolution of ISM in terms of Kerala precipitation is similar to the evolution of all-India precipitation as also shown in Fig. 4. During the ensemble mean ISM period of AERO (151 days) and CTL (161 days), total precipitation of India Peninsula is 539 mm and 571 mm, corresponding to 3.56 mm/day and 3.54 mm/day, respectively.

We further evaluate the simulated fields of circulations and precipitation against the observed climatology in three periods of the ISM evolution: pre-monsoon, developed monsoon, and withdrawal (Fig. 6). The pre-monsoon period in each of the 25 years from AERO and CTL is selected the same, i.e. March 1 to April 10 in early spring before the significant increase in monsoon rainfall (Fig. 4). Such a selection ensures that the climatological signal of seasonal transition is excluded from the difference fields of circulation between AERO and CTL assuming the climatological seasonal cycle of the two experiments is the same. For the monsoon season, we choose two and half months



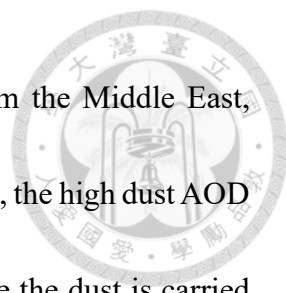
from May 26 to August 3 to define the fully developed monsoon state. The pre-monsoon and developed monsoon periods for both CTL and AERO are the same as that of the observed climatology. For the monsoon withdrawal period, we choose the four-week period centered on the withdrawal date as the transition period. So the transition period of the CTL is October 3 to November 6, the same as the observed climatology, while that of AERO is September 23 to October 27.

The observed climatological circulation and precipitation in the pre-monsoon period (Fig. 6a) indicates that the circulation in the pre-monsoon period is characterized by subtropical high over the northern Indian Ocean and surrounding land region as shown by the 500-hPa high-pressure ridge along 10°N and anticyclonic flow at 850 hPa centered around the Arabian Sea, Bay of Bengal, and the Indo-China flanked by equatorial easterlies and subtropical westerlies. Precipitation is confined to the eastern equatorial Indian Ocean and Sumatra. Following the sun in boreal summer, the climatological flow in the fully developed monsoon period shows pronounced cross-equatorial flow and the prevailing westerlies over the Indian Ocean and the Bay of Bengal. The strong westerly monsoon encounters the Indian subcontinent and Indo-China Peninsula to produce heavy monsoon rain over the western coastal regions and neighboring oceans. The associated subtropical high at 500 hPa develops a strong meridional structure with a strong anticyclonic center over the Arabian Peninsula and a cyclonic center over India and the



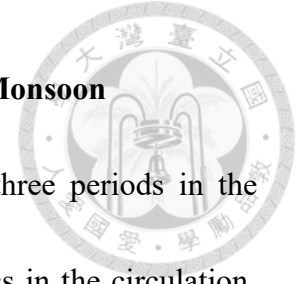
Bay of Bengal. In the monsoon withdrawal period, the overall circulation and equatorial precipitation largely resemble that of the pre-monsoon period but precipitation resides over southern India and the Bay of Bengal. This is known as the asymmetric seasonal transitions between boreal spring [March–May (MAM)] and fall [September–November (SON)] monsoon regimes, i.e. the maximum rainfall remains mostly south of the equator during boreal spring without a northwestward progression that would retrace the path of the boreal fall progression (e.g., Lau and Chan 1983; LinHo and Wang 2002; Hung et al. 2004; Chang et al. 2005). The above climatological features are reasonably simulated in AERO except for an obvious positive rainfall bias along the southern Tibetan peripheral primarily over the northern Ganges-Brahmaputra basin. The bias is most extensive in the developed monsoon and withdrawal periods. The model also overestimates rainfall in the eastern Arabian Sea and western India and underestimates rain over the Bay of Bengal in the developed monsoon period. As a result, the model-simulated southwestlies over the tropical western Indian Ocean is stronger than the observed monsoon flow.

The natural dust in Indian Peninsula is also associated with monsoon circulation. In our simulations, the AOD of Indian dust shows a seasonal cycle and has a high value from April to July (Fig. 2). We evaluate the simulated fields of dust against the observed climatology in the three periods of ISM evolution (Fig. 7). In the pre-monsoon period, high dust AOD appears over the middle Arabia Peninsula and the Tarim Basin in the



observed climatology. The monsoon circulation transports dust from the Middle East, leading to relatively high dust AOD. In the developed monsoon period, the high dust AOD appears in Arabia Peninsula and extends to northwestern India where the dust is carried by monsoon circulation into Ganges Basin and accumulated. The dust AOD decreases during monsoon withdrawal over the Arabia Peninsula to Pakistan. In addition, the Tarim Basin also shows around 0.4-0.5 AOD of dust in those three periods in the observed climatology. The climatological features of dust are also reasonably simulated in AERO except for an overestimate of dust AOD in the Tarim Basin. That is because the dry deposition and transportation in the MAM3 aerosol scheme are underestimated, leading to the overestimation of dust AOD in the source region over the Middle East and South West East (Liu et al. 2012; M. Wu et al. 2020). The overestimate is most notable in the developed monsoon.

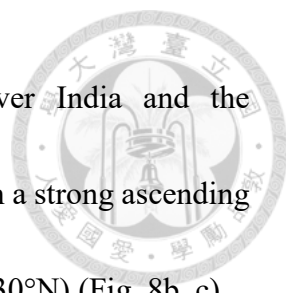
Chapter 4 Effect of anthropogenic aerosols on Indian Summer Monsoon



Based on the analysis of monsoon evaluation divided into three periods in the previous chapter, the results indicate distinct climatic characteristics in the circulation, precipitation, and aerosol distribution over the Indian region during these periods. This variation may result in aerosol effects acting through different mechanisms, leading to diverse regional impacts. In this chapter, we will delve into the effects of aerosols during each of the three periods.

4.1 Effect of anthropogenic aerosols on pre-monsoon climate

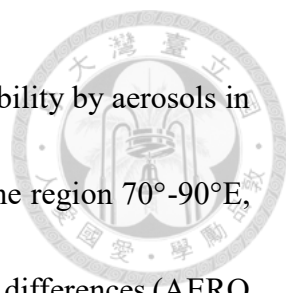
The regional circulation in the pre-monsoon period of AERO (March 1 to April 10) is shown by the ensemble-mean fields of horizontal winds and vertical velocity ($-\omega$) at 850 hPa and 500 hPa are shown in Fig. 8a and 8b, and the vertical-meridional cross-section of mean $-\omega$ within 70° - 90° E in Fig. 8c. The low-tropospheric circulation (850-hPa winds in Fig. 8a, the same as Fig. 6d) is characterized by anticyclonic flow over the Arabian Sea and Bengal-Indo China surrounded by westerlies along the southern Tibetan peripheral in 20° - 30° N and easterlies around 10° N. Associated with the circulation, deep ascending motion appears in the tropical eastern Indian Ocean as shown by positive values of $-\omega$ at 850 hPa and 500 hPa (Fig. 8a and 8b) and shallow ascending motion over India Peninsula at 850 hPa capped by descending motion at 500 hPa (Fig. 8a, b, c), indicating the emergence of a thermal low over the India Peninsula. At 500 hPa, broad



subtropical anticyclonic flow and descending motion reside over India and the neighboring Arabian Sea and Bay of Bengal that is accompanied with a strong ascending motion to the north over the southern slope of the Tibetan Plateau ($\sim 30^\circ\text{N}$) (Fig. 8b, c).

To examine the effect of anthropogenic aerosols on the pre-monsoon climate, we compare the fields of AERO against the difference fields of (AERO – CTL). First, we show the mean AOD in AERO and the differences (AERO – CTL) in Fig. 9. The figure shows that the overall suppressed condition in the lower-tropospheric anticyclonic flow (shown in Fig. 8b) in the pre-monsoon condition in AERO results in aerosols accumulation over the India Peninsula, especially downstream over eastern India and along eastern IGP without being washed out by rainfall as shown by the mean AOD (Fig. 9, shaded). The AOD differences (AERO – CTL) in Fig. 9 show the anthropogenic aerosols add further accumulations in the Ganges basin over 20° to 30°N along the southern Tibetan peripheral and over eastern India and neighboring Bay of Bengal (10° - 20°N). The distribution of AOD differences (AERO – CTL) are obviously determined by lower tropospheric winds and topography.

By absorbing and scattering solar radiation, anthropogenic aerosols generally lead to atmospheric heating and surface cooling as revealed in temperature differences (AERO – CTL) near the surface (Fig. 10a) and areal mean vertical profile of temperature (Fig. 10b) over the Indian Peninsula. The negative (positive) temperature difference near




surface (in the lower troposphere) in Fig. 10b shows an enhanced stability by aerosols in the pre-monsoon period. The surface energy budget averaged over the region 70° - 90° E, 5° - 35° N for AERO and AERO – CRL is shown in Table 3. The budget differences (AERO – CTL) are dominated by the net surface fluxes of shortwave (positive downward) and longwave (positive upward) by -7.26 W m^{-2} and -2.01 W m^{-2} , respectively. The reduced surface radiation in both downward shortwave and upward longwave is consistent with reduced surface temperature. The horizontal distribution of AOD in AERO and differences (AERO – CTL) in Fig. 9 and the vertical-meridional distribution of aerosol concentration differences (AERO – CTL) within (70° - 90° E) in Fig. 10c indicate that anthropogenic aerosols are transported by westerly and southwesterly winds (Fig. 8d and 8e) and accumulated over the terrain of Himalayas, eastern India and coastal ocean. The accumulated aerosol concentrations coincide well with the solar heating rate (Fig. 10c, shaded). Note that the heating source is all over the mountainous terrain from the foothill to the top of the Himalayas. Over 10° - 20° N, the anomalous aerosols also heat the atmosphere, but the altitude of the heating source is lower without terrain effect.

From the (AERO – CTL) differences in aerosols and solar heating (Fig. 9 and Fig. 10c), we further examine the differences in regional circulation in Fig. 8. During the pre-monsoon period, anthropogenic aerosols accumulate mostly to the east of India (Fig. 9), and the ascending motion over India Peninsula tends to shift eastwards (Fig. 8d). On the

other hand, the aerosols are transported by the southwestlies and accumulate over the foothills of the Himalayas, heating the atmosphere by absorbing solar radiation (Fig. 10c).

Elevated ascending motions over the southern slopes of the Tibetan Plateau are thermally driven by the heated atmosphere (Fig. 8e, f). The differences of horizontal and vertical flow (AERO – CTL) show a strengthening and southward expansion of upward motion from the Ganges basin to the Indian Peninsula within 70°-90°E (Fig. 8e, f), consistent with the elevated heat pump mechanism suggested in Lau et al. (2006). But the aerosols also result in zonal changes in circulation, i.e. a zonal shift of $-\omega$ in lower-tropospheric wind within 10°-20°N over the India Peninsula (Fig. 8d) and strengthened subsidence (or weakened ascending motion) west and east of the positive $-\Delta\omega$ at 500 hPa over India and Tibet within 70°-90°E. Can the aerosol-induced heating and circulation changes in the pre-monsoon period explain the variability of monsoon onsets as shown in the frequency distributions of ISM onset dates and change rate of zonal wind direction in onset in the 25 years of AERO and CTL (Fig.5)? Here we examine the co-variability of the onset date and change rate of zonal wind direction with the 500 hPa ascending motion above TP (25°-35°N, 75°-100°E) in pre-monsoon season in each of the 25 years in AERO and CTL (Fig. 11). The TP ascending motion is significantly correlated with the onset date of ISM (correlation coefficient -0.71 in AERO and -0.8 in CTL) with stronger TP ascending motion correspond to earlier onset. The TP ascending motion varies in a wider range in

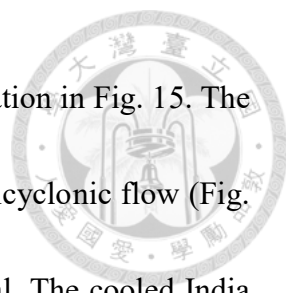


AERO (0.02 to 0.23 P s^{-1}) than in CTL (0.02 to 0.14 P s^{-1}) that is quasi-linearly related to the onset date that varies from $+13$ to -9 day in AERO and $+3$ days to -4 days in CTL and the change rate of onset that varies from 5.5 to 1 in AERO and 3 to $0.2 \text{ (m s}^{-1}\text{)}$ in CTL. So the more scattered and abrupt onset can be explained by the elevated aerosol heating over TP that altered the pre-monsoon circulation that further affect the onset. This is consistent with the conclusion that the elevated heating can change the march of ISM (Lau et al. 2006).

4.2 Effect of anthropogenic aerosols on developed monsoon climate

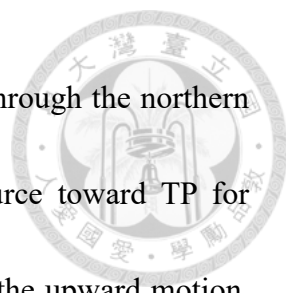
The regional circulation in the developed monsoon period of AERO (May 26 to August 3) as discussed in Chapter 3.2 (Fig. 7e) transports aerosols from Arabian Peninsula across the Arabian Sea into Indian Peninsula. As a result, the horizontal distribution of AOD in AERO (Fig. 12) shows a higher amount of aerosol over the west coast, northern India and IGP, a lower amount of aerosol over southern India and the northern Bay of Bengal due to wash out by monsoon rainfall. The ensemble-mean fields of horizontal winds and $-\omega$ at 850 hPa and 500 hPa and the vertical-meridional cross-section of mean $-\omega$ within 70° - 90°E in the developed monsoon period of AERO (May 26 to August 3) (Fig. 13) show an overall ascending motion over India subcontinent and strong cyclonic westerly monsoon flow from Arabian Sea to Bay of Bengal.

To investigate the anthropogenic aerosol-induced changes, we first show the



difference (AERO – CTL) fields of regional circulation and precipitation in Fig. 15. The cyclonic westerly monsoon flow is weakened as revealed by the anticyclonic flow (Fig. 15a, b) and reduced rainfall (Fig. 15d) over India and Bay of Bengal. The cooled India north of 20°N (Fig. 14) and heated atmosphere by aerosol is attributed to an NW-SE oriented suppressed circulation consisting of descending motion within 10°-25°N, ascending motion within 0°-10°N, and localized ascending and descending motion along the southern slope of Tibet centered within 20°-35°N (Fig. 15a,b,c). Figure 15b shows a wave pattern along the southern slope of Tibet. Analyzing the eastern (75°-85°E) and western (85°-95°E) Indian region separately (Fig. 16), the vertical profile indicates that the EHP is restricted to the western side of the TP.

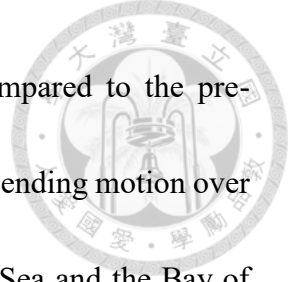
Based on the difference field of 850hPa winds (Fig. 15a, d), higher AOD over the Tibetan peripheral as revealed in the difference distribution of AOD (AERO – CTL) in Fig. 12 corresponds to northward and eastward flow at the northern portion of the anticyclonic flow over India and Bay of Bengal. The high aerosol concentration in the vertical-meridional cross-section of the corresponding difference fields within 70°-90°E coincides with solar heating above the Himalaya slope and top within 25°-35°N (Fig. 15f). Compared with the pre-monsoon period, the areas with increased anthropogenic aerosol accumulation are more concentrated on the southern slope of the plateau. Even if the washout effect occurs during the monsoon season, the daily anthropogenic aerosols that



are continuously emitted into the atmosphere will still accumulate through the northern part of the anticyclonic flow and continue to provide a heat source toward TP for atmospheric heating over the southern slope, thereby strengthening the upward motion.

In addition, a corresponding increased descending motion above the Indian Peninsula over 10° - 20° N (Fig. 15b, c) suppresses monsoon precipitation over the region (Fig. 15d), leading to a slight increase in solar heating rate (Fig. 15f).

Combining the horizontal and vertical-meridional distribution of difference fields of aerosols and circulation, the anthropogenic aerosol-induced changes in the developed monsoon appear to consist of two parts. One is an anthropogenic aerosol-induced weakened monsoon over India and the surrounding tropical oceans due to the reduced land-ocean contrast by aerosol forcing (Fig. 15e). In our experiment, SST is prescribed. Thus, when the southern Indian land surface cools by aerosols effect and the SST doesn't change by energy budget in the boundary layer, leading to a weakened land-ocean contrast with the surrounding ocean. The other part is the elevated heating and ascending motions over the southern slopes of the Tibetan Plateau due to accumulated aerosol heating (Fig. 15c, f). The ascending motions induce obviously local meridional circulation leading to a descending motion over southern India (10° - 20° N). At the same time, the anthropogenic aerosol keeps emitted leading to enhance stability in low-level by surface cooling and atmospheric heating. The descending motion above 500 hPa and the enhanced low-level



stability caused the reduced precipitation over southern India. Compared to the pre-monsoon season (Fig. 8d, e), the elevated heating also induces the ascending motion over southern TP but the descending motion is located over the Arabian Sea and the Bay of Bengal by different environmental circulation.

4.3 Moisture budget analysis in the developed monsoon period

The moisture budget analysis is used to investigate the physical mechanism of precipitation changes. The vertically integrated moisture budget equation is expressed as:

$$P' = E' - \langle V_h \cdot \nabla_h q \rangle' - \langle \omega \partial_p q \rangle' + \delta \quad (1)$$


Where P, E, q, V_h , and ω are precipitation, evaporation, specific humidity, horizontal wind, and vertical pressure velocity, respectively. $\langle \rangle$ means a vertical integration from the surface to 100 hPa. $-\langle V_h \cdot \nabla_h q \rangle'$ and $-\langle \omega \partial_p q \rangle'$ represents the changes in horizontal and vertical moisture advection, respectively. δ indicates the residual term.

The vertical moisture advection changes $-\langle \omega \partial_p q \rangle'$ in (1) can be divided into the thermodynamic, dynamic effects and nonlinear component as

$$-\langle \omega \partial_p q \rangle' = -\langle \bar{\omega} \partial_p q' \rangle - \langle \omega' \partial_p \bar{q} \rangle - \langle \omega' \partial_p q' \rangle \quad (2)$$

The thermodynamic term indicates the contribution of moisture change, while the dynamic term indicates the contribution of atmospheric circulation change.

To quantify the attribution of decadal precipitation changes, the moisture budget analysis has been performed over the South India (SI; 10°-20°N, 70°-90°E), West TP




(WTP; 25°-35°N, 75°-85°E) and East TP (ETP; 25°-35°N, 85°-95°E) in Fig. 17. The results indicate that precipitation changes are mainly attributed to vertical moisture advection in SI. Specifically, the dynamic component has preferred impacts on decadal changes in precipitation over the thermodynamic component. The result indicates that the precipitation response is mainly modulated by the anomalous subsidence above 10°-20°N in Fig. 15a-c. The precipitation changes in WTP and ETP are attributed to both horizontal and vertical moisture advection. The horizontal moisture advection contributes even more than the vertical moisture advection in ETP.

In the monsoon season, South Asian high is strengthened by the heating of the Tibetan Plateau. The summer subtropical Asian westerly jet (AWJ) extends to south. The westerly component of the circulation blowing into the WTP increases, causing more moisture to be transported from the Indian Ocean to the WTP. At this point, the WTP becomes a windward side where the moisture converges.

In the moisture budget, horizontal moisture advection is equally important as vertical moisture advection. The 500hPa moisture divergence anomaly reveals that in the WTP (Fig. 18), besides the increased precipitation due to the strengthened vertical circulation, horizontal advection of moisture also contributes importantly to precipitation in this region.

The southern edge of the TP exhibits an east-west asymmetry in its topography.

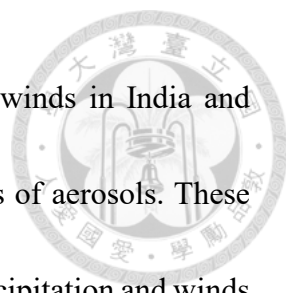


When the lower-level westerly circulation strengthens and transports moisture towards the TP, the WTP becomes the windward side while the ETP transitions to the leeward side. After moisture convergence and rainfall in the WTP, the circulation entering the ETP no longer carries a significant amount of moisture, leading to reduced precipitation in that area. Previous studies have also indicated the complex nature of the terrain along the southern edge of the TP, making it challenging for models to accurately capture, resulting in an overestimation of the residue term in the moisture budget analysis.

4.4 Effect of anthropogenic aerosols on monsoon withdrawal and post-monsoon climate

For the monsoon withdrawal period, we choose the four-week period centered at the withdrawal date as the transition period that is further divided into two: the two weeks before the withdrawal date as Phase-1 and the two weeks after as Phase+1. The Phase-1, withdrawal date, and Phase+1 correspond to (Oct. 3 to Oct. 18), October 20, and (Oct. 22 to Nov. 6) for CTL, and (Sep. 23 to Oct. 8), October 10, and (Oct. 12 to Oct. 27) for AERO, respectively.

The ensemble-mean AOD, 850 hPa winds, and precipitation in the Phase-1 and Phase+1 of AERO and CTL are shown in Fig. 19 and Fig. 20. The figures show a clear weakening and southward shift of the cyclonic Indian monsoon flow and rainfall, and a strengthening of the subtropical high over Indo-China from Phase-1 to Phase+1. The



above circulation transition leads to a change of low-tropospheric winds in India and Arabian Sea from westerly to easterly and the consequent transports of aerosols. These changes in transition are better revealed by the difference fields of precipitation and winds (Phase+1 minus Phase-1) in Fig. 22a. The difference fields show anticyclonic flow and suppressed rainfall within 10°-30°N, cyclonic flow and enhanced rainfall within 0°-10°N. Persistent easterlies reside within 10°-20°N between the two zonal bands of anticyclonic and cyclonic flow. The aerosol effect in withdrawal period continues to exert its influence in the region north of 15°N in India by surface cooling (Fig. 21d) and atmosphere heating (Fig. 21e), leading to the persistent presence of anticyclonic anomalies over the eastern coastline. The heating effect of aerosols on the atmosphere is confined to the boundary layer in the river valley regions (Fig. 21e).

The change in aerosol transport and the weakening rainfall washout result in more anthropogenic aerosol accumulation over the IGP and westward expansion of AOD over the Indian Peninsula from Phase-1 to Phase+1 (Fig. 19). The change of AOD distribution in the transition phases also shows in the AOD differences (AERO – CTL), i.e. the contours and shadings in Fig. 19 resemble each other, indicating the changes are primarily anthropogenic origin.

The influences of anthropogenic aerosols on the monsoon transition are shown by the difference fields of precipitation and winds (AERO minus CTL) for Phase-1 and

Phase+1 (Fig. 22b). The figure shows an anticyclonic flow from Indo-China to eastern India within 10° - 25° N and cyclonic flow over the eastern Indian Ocean within 0° - 10° N.

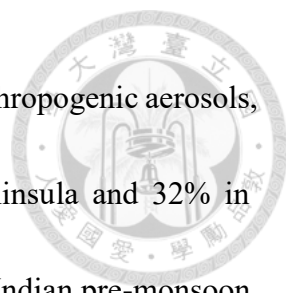
The aerosol-induced changes in Fig. 22b largely resemble the transition changes east of 80° E in Fig. 22a. This is attributed to the earlier withdrawal in AERO relative to CTL.

Such an anthropogenic aerosol influence on monsoon evolution is consistent with Chen et al. (2018) who attributed post-monsoon precipitation reduction over South Asia to aerosols.

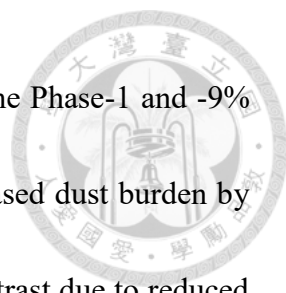
Chapter 5 Circulation changed influence on natural dust distribution in monsoon evolution



In our experiments, we apply the same dust emission data (The year 1850) in both CTL and AERO so that the desertification effect is excluded to simplify the experiment. Even the anthropogenic aerosols are the only variation in our study, dust emission can be changed by surface wind speed in the model, leading to differences of dust distribution by circulation change induced by anthropogenic aerosols. We evaluate the influences of dust distribution under anthropogenic-aerosol-induced circulation change in simulations. The dust AOD differences with a confidence level greater than 90% are shown in Fig. 23 and with 850hPa wind field differences. In the pre-monsoon period, the dust AOD increases in the northwest side of the anthropogenic-aerosol-induced anomalous anticyclone above the Arabia Sea, inducing the transportation of dust from middle Arabia to Pakistan. The dust AOD increases about 20% in middle Arabia and southeastern Pakistan (Fig. 23a). More natural dust is transported along the topography into the Ganges Valley from the Middle East under anthropogenic aerosol-induced circulation change during the pre-monsoon period. For differences of aerosols in the Indian Peninsula (70° - 90° E, 5° - 35° N), the concentration of BC increases 60%, OC increases 17%, sulfate increases 7% and dust also increases 16% in total aerosols (Table 4). Natural dust can heat the atmosphere and cool the surface by radiation absorption which is similar to the



effect of BC and OC. Calculating the differences AOD of dust and anthropogenic aerosols, the dust contributes 26% in increased total AOD over Indian Peninsula and 32% in northern India (Table 5). As a result, the local climate change in the Indian pre-monsoon period may have about 1/3 of the contribution by dust. The anthropogenic-aerosol-induced anticyclonic flow over the Indian Peninsula results in suppressed conditions and weakened monsoon that causes a decreased transportation of dust from Arabia in the developed monsoon period (Fig. 23b). In the Indian developed monsoon period, the part of changes in the dust is negligibly small, the dust concentration differences decrease 0.34% (Table 4), and the corresponding AOD differences decrease 3% (Table 5). Indeed, the anthropogenic aerosols dominate the local climate change by radiation budget changes as discussed in Chapter 5. In the first half of the withdrawal period (phase-1), the dust AOD increases 21% over the western Arabian Sea and the southern coast of the Arabian Peninsula. The increased dust AOD is limited to the west of the sea by the anomalous easterly wind over the Bay of Bengal and southern India in 10°-20°N (Fig. 23c). In the second half of the withdrawal period (phase+1), the differences of dust AOD are only located over the Middle East and the Arabian Peninsula because of the anticyclonic anomalous above India and strengthened easterlies over 10°N (Fig. 23d). The Indian aerosol concentration differences of dust in the atmosphere increases 0.37% in the Phase-1 and decreases 0.34% in the Phase+1 (Table 4). For the total AOD



differences over India, the dust AOD differences contribute 6% in the Phase-1 and -9% in the Phase+1 (Table 5). According to Wei et al. (2022), the decreased dust burden by the easterly wind anomalies is a result of the meridional heating contrast due to reduced (increased) BC burden over northern (southern) India in April and May. In our study, the meridional asymmetrical heating of the atmosphere in India is opposite to Wei et al. (2022). The atmospheric heating by anthropogenic aerosols in the north of 20°N is greater and higher than the south (Fig. 10b) by topography effect that cause an opposite pressure gradient force in our study. The westerly wind anomalies which is opposite to Wei et al. (2022) bring more dust from the Middle East in pre-monsoon period. In developed monsoon period, the atmospheric heating concentrates in the southern slope of TP and the overall India is suppressed (Fig. 15a-c) that the opposite anomalous meridional heating of atmosphere disappeared. The suppressed phase extends to withdrawal period that cause the weakened transportation of dust from the Middle East to India during developed period to withdrawal. As a result, the anthropogenic aerosols may have a major effect on local climate over India from developed period to withdrawal in this study. However, the natural dust coming from the Arabian Peninsula is also important to the local climate change over India in the pre-monsoon period, even if the anthropogenic-aerosol-induced circulation change influences more on the distribution of dust over upstream of dust transportation.

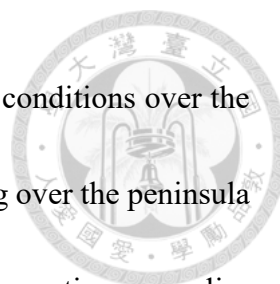


Chapter 6 Discussion

Overall, the increased anthropogenic aerosol emissions lead to a more stable lower troposphere by aerosol-radiative forcing in India Peninsula by aerosol dimming effects in all three period. But the temperature differences between India and surrounding ocean is significantly enhanced by aerosols in the pre-monsoon period but not in the following periods. Furthermore, the aerosol-induced elevated heating over Tibet differs in the pre-monsoon and developed monsoon periods. The differences are assumed to be the responses to the elevated heating in the different mean flows. The elevated heating and aerosol dimming also affects the timing and change rate of ISM onset. More specific discussions follows.

6.1 Comparison of the EHP and dimming effect over India


Aerosol-induced atmospheric heating over the Indian Peninsula is greater in the pre-monsoon period compared to the developed monsoon and withdrawal periods. This results in a larger atmospheric temperature gradient between land (70° - 90° E, 10° - 20° N) and the surrounding ocean (70° - 90° E, 0° - 10° N) during the pre-monsoon period in the Indian region (Table 6). In the pre-monsoon period, the aerosol effect leads to an average increase of 2.3° C in atmospheric temperature over land and a 0.4° C increase over the ocean, and a cooling of 0.32° C in land surface. Consequently, the average atmospheric temperature over the land becomes 25.3° C, while 22.6° C over the ocean, resulting in a



land-sea temperature gradient of 2.7°C . As a result, the atmospheric conditions over the peninsula favor enhanced ascending motion. The atmospheric heating over the peninsula and the significant effect of the EHP contributed to increased ascending motion anomalies over the Indian region during the pre-monsoon period.

During the developed monsoon, the prevailing wind field, including westerly and southerly components, causes the aerosol distribution to shift northward. The aerosol concentration decreased by the northward transported and rainfall washout effect over the peninsula. The average atmospheric heating over the Indian Peninsula at 850hPa is 0.9°C , and 0.3°C over the ocean, and a cooling of 0.28°C in land surface. The atmospheric temperature gradient between land and ocean is smaller (0.7°C) and the land surface experiences cooling due to the dimming effect (Fig. 21d). This leads to stable atmospheric conditions over the Indian Peninsula, accompanied by the generation of anticyclonic anomalies. The EHP over the Northern Indian Plateau (Fig. 15f) is limited to western TP.

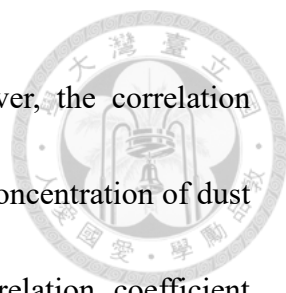
In the withdrawal period, aerosol distribution concentrates in the Ganges River Valley plain, with the aerosol effect causing localized heating limited to below 850hPa north of 20°N . The atmospheric average warming over the Indian Peninsula is 0.7°C and 0.3°C over the ocean, and the land surface average cooling is 0.41°C . The atmospheric temperature over the ocean is slightly higher than over the land by 0.2°C . Due to the relatively small land-sea temperature gradient and the slightly higher atmospheric



temperature over the ocean, the Indian Peninsula is less conducive to the enhancement of ascending motion. Additionally, the simultaneous action of the dimming effect maintains an anticyclonic anomaly at 850hPa over the Indian Peninsula, accompanied by strengthened descending motion.

6.2 The larger variability of onset date in AERO

Based on the results from Chapter 4, the onset date distribution in each year of the AERO is more spread out compared to the CTL. We attribute the larger variability in onset dates to the distribution of anthropogenic aerosols and imported dust above 850hPa in the upper atmosphere. According to the results presented in Chapter 4.1, there is a positive correlation between the onset date and the 500hPa ascending motion along the southern edge of the TP (25°-35°N, 70°-90°E). As aerosols are transported by the circulation towards the plateau and contribute to atmospheric warming through the aerosol effect in the mid-level atmosphere, this further enhances ascending motion. Therefore, we further analyze the relationship between the average aerosol concentration in the mid-level atmosphere (850-500hPa) and ascending motion. The correlation analysis between the average concentrations of dust and anthropogenic aerosols in the mid-level atmosphere and the 500hPa Tibetan Plateau ascending motion is illustrated in Fig. 24. Higher concentrations of anthropogenic aerosols in the mid-level atmosphere correspond to larger ascending motion. The correlation coefficient between



anthropogenic aerosols and TP ascending motion is 0.77. However, the correlation coefficient between dust and TP ascending motion is -0.49. Higher concentration of dust corresponds to smaller ascending motion. Furthermore, the correlation coefficient between dust and TP ascending motion in CTL (without anthropogenic aerosols) is -0.55 (not shown). This result suggests that the larger variability in the onset date in the AERO may be simultaneously influenced by the concentrations of mid-level dust and anthropogenic aerosols. Anthropogenic aerosols are positively correlated with TP ascending motion, but the intensity of TP ascending motion influenced by anthropogenic aerosols is mitigated by the inhibitory effects of dust. Additionally, the concentration of dust transported from the Middle East to Northern India varies significantly each year. The transported dust from the Middle East into Northern India typically has a higher altitude distribution. When higher concentrations of dust are situated above anthropogenic aerosols, the optical properties of dust, affecting radiative scattering and refraction, weaken the efficiency of anthropogenic aerosols in absorbing radiation and heating the atmosphere. This, in turn, further influences the intensity of ascending motion.




Chapter 7 Summary

In this study, NCAR CAM 5.1 is used to study the influences of aerosol direct effect on regional monsoon evolution by the control (CTL) and aerosol (AERO) experiments that differ by annual mean distribution of anthropogenic emissions over India Peninsula within (70°-95°E, 5°-35°N) with an area average of 1.77 Mg m⁻² month⁻¹. The two experiments are integrated for 30 years subject to the same perpetual SST annual cycle. The model reasonably simulates the overall monsoon evolution except the positive bias in rainfall over the northern Ganges-Brahmaputra basin, stronger westerly monsoon over tropical western Indian Ocean and the downstream rainfall near western India.

Our analysis of the differences of the two experiments shows that the transition of the ISM from spring to fall in AERO exhibits a similar ensemble-mean onset date with larger spread and more abrupt change, and an earlier but more gradual withdrawal relative the ISM evolution in AERO. To further summarize the effect of aerosols on the overall ISM evolution in study, we note that previous studies have provided a background knowledge that anthropogenic emissions over India alter the radiative flux distribution causing atmospheric heating and surface cooling that leads to a general tendency of weaker ISM. But the ISM responses to aerosol radiative forcing are further changed by advection, topography, and rainfall washout.


The AOD differences between the two experiments (AERO – CTL) show a common



feature of aerosol accumulations in Ganges-Brahmaputra basin over 20° to 30°N from spring to fall. The difference fields show additional regions of high AOD in the three stages of monsoon evolution: eastern India and neighboring Bay of Bengal (10°-20°N) in the pre-monsoon period; northeast India in the developed monsoon; northeast India and neighboring Arabia Sea in the period after monsoon withdrawal (post-monsoon).

In the pre-monsoon environment, aerosols lead to stronger upward motion from Tibet through the Ganges basin to the Indian Peninsula within 70°-90°E along with strengthened anticyclonic circulation over the Arabia Sea and eastern Bay of Bengal and a zonal shift of lower-tropospheric wind within 10°-20°N. The strengthened anticyclonic flow caused an increased natural dust transport from the Middle East. Furthermore, those changes in circulation are well correlated with the dates and change rates of ISM onset, i.e. the stronger TP ascending motion in the pre-monsoon period corresponds to earlier and more abrupt onset. On the other hand, anthropogenic aerosol concentration on the TP is positively correlated with TP ascending motion, while dust concentration shows a negative correlation with TP ascending motion. This causal correlation supports the explanation that the aerosol-induced elevated heating over Tibet causes enhanced meridional overturning circulation that further causes more spread in ISM onset dates and more abrupt transitions in ISM onset. Other factors like intraseasonal variability can also influence the ISM evolution to cause more scattered onsets. These possible causes await


further studies.



In the developed monsoon period, aerosols result in weakened cyclonic westerly monsoon flow and rainfall over India and Bay of Bengal but a stronger NW-SE oriented band of ascending motion within 0° - 10° N (ITCZ). Aerosols also lead to localized ascending along the southern slope of Tibet around 75° - 85° E and 30° N due to atmospheric heating that corresponds to high concentrations of aerosols transported by anticyclonic anomalies. The localized ascending motion is limited to western TP presumably due to weakened land-sea contrast by aerosols over India and the terrain effect of the TP. The former causes an anomalous anticyclonic flow that transport moisture to the western TP by its southwestern component flow. The terrain effect of the TP leads to increased ascending motion on the windward side (western TP) and descending motion on the leeward side (eastern TP).

The influences of aerosols on monsoon withdrawal feature a tendency to form anticyclonic flow from Indo-China to eastern India within 10° - 25° N and cyclonic flow over eastern Indian Ocean within 0° - 10° N. The aerosol-induced changes resemble the transitional changes in monsoon withdrawal over eastern India and Bay of Bengal. This helps to explain the earlier monsoon withdrawal in AERO relative to CTL, consistent with the finding in Chen et al. (2018).

We only show experiments with aerosol direct effect in this report although we did



carry out experiments including aerosol indirect effect on Indian monsoon that is not reported here because of large uncertainties in the treatment of aerosol-cloud interactions in the model. With only aerosol direct effect in the model, our results summarized above are in general agreement with those studies using coupled ocean-atmosphere climate models with more careful treatment of aerosol forcing (e.g. Ramanathan et al., 2005).

Similar to Lau et al. (2006), the SST annual cycle is prescribed in the model and our experiments show aerosols in pre-monsoon period lead to stronger upward motion over the Ganges basin and the southern slope of Tibetan Plateau by accumulation and induce the meridional overturning that is similar to the results in Lau et al. (2006) and Lau and Kim (2006) who suggested the EHP theory as the cause. Note however that the spatial and temporal distribution of the meridional overturning circulation over Indian subcontinent in pre-monsoon period in this study bears notable differences from the results in Lau et al. (2006) as discussed in Chapter 4. A likely cause is the different treatment of aerosol forcing that is motion dependent in our study but fixed in Lau et al. (2006).

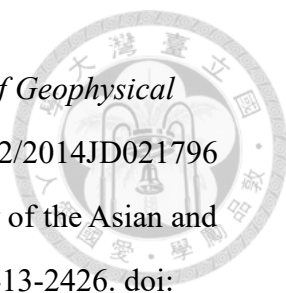


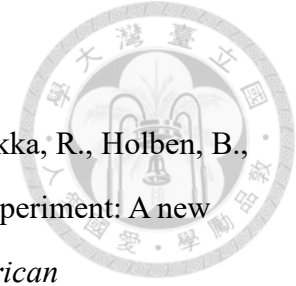
Reference

- Annamalai, H., Hafner, J., Sooraj, K., & Pillai, P. (2013). Global warming shifts the monsoon circulation, drying South Asia. *Journal of Climate*, 26(9), 2701-2718. doi:10.1175/JCLI-D-12-00208.1
- Badarinath, K., Kharol, S. K., Kaskaoutis, D., Sharma, A. R., Ramaswamy, V., & Kambezidis, H. (2010). Long-range transport of dust aerosols over the Arabian Sea and Indian region—A case study using satellite data and ground-based measurements. *Global and Planetary Change*, 72(3), 164-181.
- Bollasina, M., Nigam, S., & Lau, K. (2008). Absorbing aerosols and summer monsoon evolution over South Asia: An observational portrayal. *Journal of Climate*, 21(13), 3221-3239. doi:10.1175/2007JCLI2094.1
- Bollasina, M. A., Ming, Y., & Ramaswamy, V. (2011). Anthropogenic aerosols and the weakening of the South Asian summer monsoon. *Science*, 334(6055), 502-505. doi:10.1126/science.1204994
- Bollasina, M. A., Ming, Y., & Ramaswamy, V. (2013). Earlier onset of the Indian monsoon in the late twentieth century: The role of anthropogenic aerosols. *Geophysical Research Letters*, 40(14), 3715-3720. doi:10.1002/grl.50719
- Bretherton, C. S., & Park, S. (2009). A new moist turbulence parameterization in the Community Atmosphere Model. *Journal of Climate*, 22(12), 3422-3448. doi:10.1175/2008JCLI2556.1
- Chang, C.-P., Wang, Z., McBride, J., & Liu, C.-H. (2005). Annual cycle of Southeast Asia—Maritime Continent rainfall and the asymmetric monsoon transition. *Journal of Climate*, 18(2), 287-301. doi:10.1175/JCLI-3257.1
- Chen, W.-T., Huang, K.-T., Lo, M.-H., & LinHo, L. (2018). Post-Monsoon Season Precipitation Reduction over South Asia: Impacts of Anthropogenic Aerosols and Irrigation. *Atmosphere*, 9(8). doi:10.3390/atmos9080311
- Cheng, Q., & Zhou, T. (2014). Multidecadal variability of North China aridity and its relationship to PDO during 1900–2010. *Journal of Climate*, 27(3), 1210-1222.




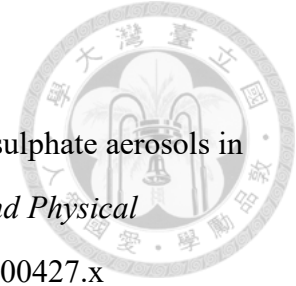
- doi:10.1175/JCLI-D-13-00235.1
- Chung, C. E., & Ramanathan, V. (2006). Weakening of North Indian SST gradients and the monsoon rainfall in India and the Sahel. *Journal of Climate*, 19(10), 2036-2045. doi:10.1175/JCLI3820.1
- Cowan, T., & Cai, W. (2011). The impact of Asian and non-Asian anthropogenic aerosols on 20th century Asian summer monsoon. *Geophysical Research Letters*, 38(11). doi:10.1029/2011GL047268
- Ding, Y., Sun, Y., Wang, Z., Zhu, Y., & Song, Y. (2009). Inter-decadal variation of the summer precipitation in China and its association with decreasing Asian summer monsoon Part II: Possible causes. *International Journal of Climatology: A Journal of the Royal Meteorological Society*, 29(13), 1926-1944. doi:10.1002/joc.1759
- Ding, Y., Wang, Z., & Sun, Y. (2008). Inter-decadal variation of the summer precipitation in East China and its association with decreasing Asian summer monsoon. Part I: Observed evidences. *International Journal of Climatology: A Journal of the Royal Meteorological Society*, 28(9), 1139-1161. doi:10.1002/joc.1615
- Ganguly, D., Rasch, P. J., Wang, H., & Yoon, J. H. (2012). Climate response of the South Asian monsoon system to anthropogenic aerosols. *Journal of Geophysical Research: Atmospheres*, 117(D13). doi:10.1029/2012JD017508
- Goyal, M. K. (2014). Statistical analysis of long term trends of rainfall during 1901–2002 at Assam, India. *Water resources management*, 28(6), 1501-1515. doi:10.1007/s11269-014-0529-y
- Guo, J., Deng, M., Lee, S. S., Wang, F., Li, Z., Zhai, P., Liu, H., Lv, W., Yao, W., & Li, X. (2016). Delaying precipitation and lightning by air pollution over the Pearl River Delta. Part I: Observational analyses. *Journal of Geophysical Research: Atmospheres*, 121(11), 6472-6488. doi:10.1002/2015JD023257
- Huang, J., Wang, T., Wang, W., Li, Z., & Yan, H. (2014). Climate effects of dust

- 
- aerosols over East Asian arid and semiarid regions. *Journal of Geophysical Research: Atmospheres*, 119(19), 11,398-311,416. doi:10.1002/2014JD021796
- Hung, C.-w., Liu, X., & Yanai, M. (2004). Symmetry and asymmetry of the Asian and Australian summer monsoons. *Journal of Climate*, 17(12), 2413-2426. doi:10.1175/1520-0442(2004)017<2413:SAAOTA>2.0.CO;2
- Iacono, M. J., Delamere, J. S., Mlawer, E. J., Shephard, M. W., Clough, S. A., & Collins, W. D. (2008). Radiative forcing by long-lived greenhouse gases: Calculations with the AER radiative transfer models. *Journal of Geophysical Research: Atmospheres*, 113(D13). doi:10.1029/2008JD009944
- Jiang, J., & Zhou, T. (2019). Global monsoon responses to decadal sea surface temperature variations during the twentieth century: Evidence from AGCM simulations. *Journal of Climate*, 32(22), 7675-7695. doi:10.1175/JCLI-D-18-0890.1
- Krishnan, R., Sabin, T., Ayantika, D., Kitoh, A., Sugi, M., Murakami, H., Turner, A., Slingo, J., & Rajendran, K. (2013). Will the South Asian monsoon overturning circulation stabilize any further? *Climate Dynamics*, 40(1-2), 187-211. doi:10.1007/s00382-012-1317-0
- Krishnan, R., Sabin, T., Vellore, R., Mujumdar, M., Sanjay, J., Goswami, B., Hourdin, F., Dufresne, J.-L., & Terray, P. (2016). Deciphering the desiccation trend of the South Asian monsoon hydroclimate in a warming world. *Climate Dynamics*, 47(3), 1007-1027. doi:10.1007/s00382-015-2886-5
- Krishnan, R., & Sugi, M. (2003). Pacific decadal oscillation and variability of the Indian summer monsoon rainfall. *Climate Dynamics*, 21(3-4), 233-242. doi:10.1007/s00382-003-03
- Lamarque, J.-F., Bond, T. C., Eyring, V., Granier, C., Heil, A., Klimont, Z., Lee, D., Liousse, C., Mieville, A., & Owen, B. (2010). Historical (1850–2000) gridded anthropogenic and biomass burning emissions of reactive gases and aerosols: methodology and application. *Atmospheric Chemistry and Physics*, 10(15),




- 7017-7039. doi:10.5194/acp-10-7017-2010
- Lau, K.-M., Ramanathan, V., Wu, G.-X., Li, Z., Tsay, S., Hsu, C., Sikka, R., Holben, B., Lu, D., & Tartari, G. (2008). The Joint Aerosol–Monsoon Experiment: A new challenge for monsoon climate research. *Bulletin of the American Meteorological Society*, 89(3), 369-384. doi:10.1175/BAMS-89-3-369
- Lau, K. M., & Kim, K. M. (2006). Observational relationships between aerosol and Asian monsoon rainfall, and circulation. *Geophysical Research Letters*, 33(21). doi:10.1029/2006gl027546
- Lau, K. M., Kim, M. K., & Kim, K. M. (2006). Asian summer monsoon anomalies induced by aerosol direct forcing: the role of the Tibetan Plateau. *Climate Dynamics*, 26(7-8), 855-864. doi:10.1007/s00382-006-0114-z
- Lau, K.-M., & Chan, P. H. (1983). Short-term climate variability and atmospheric teleconnections from satellite-observed outgoing longwave radiation. Part I: Simultaneous relationships. *Journal of the atmospheric sciences*, 40(12), 2735-2750. doi:10.1175/1520-0469(1983)040<2735:STCVAA>2.0.CO;2
- Lau, W. K. M., Kim, K. M., Shi, J. J., Matsui, T., Chin, M., Tan, Q., Peters-Lidard, C., & Tao, W. K. (2017). Impacts of aerosol-monsoon interaction on rainfall and circulation over Northern India and the Himalaya Foothills. *Clim Dyn*, 49, 1945-1960. doi:10.1007/s00382-016-3430-y
- Lau, W. K. M., Kim, K.-M., Chern, J.-D., Tao, W. K., & Leung, L. R. (2019). Structural changes and variability of the ITCZ induced by radiation–cloud–convection–circulation interactions: inferences from the Goddard Multi-scale Modeling Framework (GMMF) experiments. *Climate Dynamics*, 54(1-2), 211-229. doi:10.1007/s00382-019-05000-y
- Lawrence, D. M., et al. (2011), Parameterization improvements and functional and structural advances in version 4 of the Community Land Model, *J. Adv. Model. Earth Syst.*, 3, M03001, doi:10.1029/2011MS000045.
- Lee, J.-Y., & Wang, B. (2014). Future change of global monsoon in the CMIP5. *Climate*

- 
- Dynamics*, 42(1-2), 101-119. doi:10.1007/s00382-012-1564-0
- Li, Z. (2004). Aerosol and Climate: A Perspective from East Asia, Observation, Theory and Modeling of Atmospheric Variability. *World Sci., Hackensack, NJ*, 501-525.
- Li, Z., Chen, H., Cribb, M., Dickerson, R., Holben, B., Li, C., Lu, D., Luo, Y., Maring, H., & Shi, G. (2007a). Preface to special section on East Asian Studies of Tropospheric Aerosols: An International Regional Experiment (EAST-AIRE). *Journal of Geophysical Research: Atmospheres*, 112(D22). doi:10.1029/2007JD008853
- Li, Z., Lau, W. K. M., Ramanathan, V., Wu, G., Ding, Y., Manoj, M. G., Liu, J., Qian, Y., Li, J., Zhou, T., Fan, J., Rosenfeld, D., Ming, Y., Wang, Y., Huang, J., Wang, B., Xu, X., Lee, S. S., Cribb, M., Zhang, F., Yang, X., Zhao, C., Takemura, T., Wang, K., Xia, X., Yin, Y., Zhang, H., Guo, J., Zhai, P. M., Sugimoto, N., Babu, S. S., & Brasseur, G. P. (2016). Aerosol and monsoon climate interactions over Asia. *Reviews of Geophysics*, 54(4), 866-929. doi:10.1002/2015rg000500
- Li, Z., Li, C., Chen, H., Tsay, S. C., Holben, B., Huang, J., Li, B., Maring, H., Qian, Y., & Shi, G. (2011a). East Asian studies of tropospheric aerosols and their impact on regional climate (EAST-AIRC): An overview. *Journal of Geophysical Research: Atmospheres*, 116(D7). doi:10.1029/2010JD015257
- Li, Z., Niu, F., Fan, J., Liu, Y., Rosenfeld, D., & Ding, Y. (2011b). Long-term impacts of aerosols on the vertical development of clouds and precipitation. *Nature geoscience*, 4(12), 888-894. doi:10.1038/NGEO
- LinHo, & Wang, B. (2002). The time–space structure of the Asian–Pacific summer monsoon: A fast annual cycle view. *Journal of Climate*, 15(15), 2001-2019. doi:10.1175/1520-0442(2002)015<2001:TTSSOT>2.0.CO;2
- Liu, X., Easter, R. C., Ghan, S. J., Zaveri, R., Rasch, P., Shi, X., Lamarque, J.-F., Gettelman, A., Morrison, H., & Vitt, F. (2012). Toward a minimal representation of aerosols in climate models: Description and evaluation in the Community Atmosphere Model CAM5. *Geoscientific Model Development*, 5(3), 709-739.



- doi:10.5194/gmd-5-709-2012
- Liu, Y., Sun, J., & Yang, B. (2009). The effects of black carbon and sulphate aerosols in China regions on East Asia monsoons. *Tellus B: Chemical and Physical Meteorology*, 61(4), 642-656. doi:10.1111/j.1600-0889.2009.00427.x
- Meehl, G. A., Arblaster, J. M., & Collins, W. D. (2008). Effects of black carbon aerosols on the Indian monsoon. *Journal of Climate*, 21(12), 2869-2882. doi:10.1175/2007JCLI1777.1
- Menon, S., Hansen, J., Nazarenko, L., & Luo, Y. (2002). Climate effects of black carbon aerosols in China and India. *Science*, 297(5590), 2250-2253. doi:10.1126/science.1075159
- Morrison, H., & Gettelman, A. (2008). A new two-moment bulk stratiform cloud microphysics scheme in the Community Atmosphere Model, version 3 (CAM3). Part I: Description and numerical tests. *Journal of Climate*, 21(15), 3642-3659. doi:10.1175/2008JCLI2105.1
- Nakajima, T., Yoon, S. C., Ramanathan, V., Shi, G. Y., Takemura, T., Higurashi, A., Takamura, T., Aoki, K., Sohn, B. J., & Kim, S. W. (2007). Overview of the Atmospheric Brown Cloud East Asian Regional Experiment 2005 and a study of the aerosol direct radiative forcing in east Asia. *Journal of Geophysical Research: Atmospheres*, 112(D24). doi:10.1029/2007JD009009
- Neale, R. B., Chen, C.-C., Gettelman, A., Lauritzen, P. H., Park, S., Williamson, D. L., Conley, A. J., Garcia, R., Kinnison, D., & Lamarque, J.-F. (2010). Description of the NCAR community atmosphere model (CAM 5.0). *NCAR Tech. Note NCAR/TN-486+ STR*, 1(1), 1-12.
- Oleson, K. W., Lawrence, D. M., Bonan, G. B., Flanner, M. G., Kluzek, E., Lawrence, P. J., Levis, S., Swenson, S. C., Thorn, P. E. (2010), Technical description of version 4.0 of the Community Land Model (CLM), *NCAR Tech. Note NCAR/TN-478+STR*, 257 pp., Natl. Cent. for Atmos. Res., Boulder, Colo. doi:10.5065/D6FB50WZ

- 
- Park, S. (2010). Revised stratiform macrophysics in the Community Atmosphere Model. *J. Clim.*
- Park, S., & Bretherton, C. S. (2009). The University of Washington shallow convection and moist turbulence schemes and their impact on climate simulations with the Community Atmosphere Model. *Journal of Climate*, 22(12), 3449-3469.
doi:10.1175/2008JCLI2557.1
- Praveen, B., Talukdar, S., Mahato, S., Mondal, J., Sharma, P., Islam, A. R. M. T., & Rahman, A. (2020). Analyzing trend and forecasting of rainfall changes in India using non-parametrical and machine learning approaches. *Scientific reports*, 10(1), 1-21. doi:10.1038/s41598-020-67228-7
- Ramanathan, V., & Carmichael, G. (2008). Global and regional climate changes due to black carbon. *Nature geoscience*, 1(4), 221-227.
- Ramanathan, V., Chung, C., Kim, D., Bettge, T., Buja, L., Kiehl, J. T., Washington, W. M., Fu, Q., Sikka, D. R., & Wild, M. (2005). Atmospheric brown clouds: Impacts on South Asian climate and hydrological cycle. *Proceedings of the National Academy of Sciences*, 102(15), 5326-5333.
doi:10.1073/pnas.0500656102
- Ramanathan, V., Crutzen, P. J., Lelieveld, J., Mitra, A., Althausen, D., Anderson, J., Andreae, M., Cantrell, W., Cass, G., & Chung, C. (2001b). Indian Ocean Experiment: An integrated analysis of the climate forcing and effects of the great Indo-Asian haze. *Journal of Geophysical Research: Atmospheres*, 106(D22), 28371-28398. doi:10.1029/2001JD900133
- Rosenfeld, D. (2000). Suppression of rain and snow by urban and industrial air pollution. *Science*, 287(5459), 1793-1796. doi:10.1126/science.287.5459.1793
- Roxy, M. K., Ritika, K., Terray, P., Murtugudde, R., Ashok, K., & Goswami, B. (2015). Drying of Indian subcontinent by rapid Indian Ocean warming and a weakening land-sea thermal gradient. *Nature communications*, 6(1), 1-10.
doi:10.1038/ncomms8423



Sabeerali, C., & Ajayamohan, R. (2017). On the shortening of Indian summer monsoon season in a warming scenario. *Climate Dynamics*, 50(5), 1609-1624.

doi:10.1007/s00382-017-37

Salzmann, M., & Cherian, R. (2015). On the enhancement of the Indian summer monsoon drying by Pacific multidecadal variability during the latter half of the twentieth century. *Journal of Geophysical Research: Atmospheres*, 120(18), 9103-9118.

doi:10.1002/2015JD023313

Salzmann, M., Weser, H., & Cherian, R. (2014). Robust response of Asian summer monsoon to anthropogenic aerosols in CMIP5 models. *Journal of Geophysical Research: Atmospheres*, 119(19), 11,321-311,337.

doi:10.1002/2014JD021783

Satheesh, S., & Srinivasan, J. (2002). Enhanced aerosol loading over Arabian Sea during the pre-monsoon season: Natural or anthropogenic? *Geophysical Research Letters*, 29(18), 21-21-21-24.

doi:10.1029/2002GL015687

Shi, H., Wang, B., Cook, E. R., Liu, J., & Liu, F. (2018). Asian summer precipitation over the past 544 years reconstructed by merging tree rings and historical documentary records. *Journal of Climate*, 31(19), 7845-7861.

doi:10.1175/JCLI-D-18-0003.1

Stocker, T. (2014). *Climate change 2013: the physical science basis: Working Group I contribution to the Fifth assessment report of the Intergovernmental Panel on Climate Change*. Cambridge university press.

Wang, B., Biasutti, M., Byrne, M. P., Castro, C., Chang, C.-P., Cook, K., Fu, R., Grimm, A. M., Ha, K.-J., Hendon, H., Kitoh, A., Krishnan, R., Lee, J.-Y., Li, J., Liu, J., Moise, A., Pascale, S., Roxy, M. K., Seth, A., Sui, C.-H., Turner, A., Yang, S.,

Yun, K.-S., Zhang, L., & Zhou, T. (2021). Monsoons Climate Change

Assessment. *Bulletin of the American Meteorological Society*, 102(1), E1-E19.

doi:10.1175/bams-d-19-0335.1.

Wang, B., Huang, F., Wu, Z., Yang, J., Fu, X., & Kikuchi, K. (2009). Multi-scale climate variability of the South China Sea monsoon: A review. *Dynamics of*

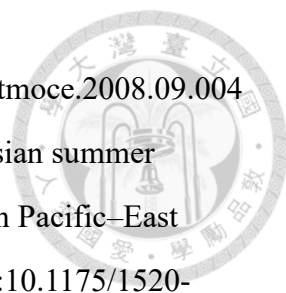
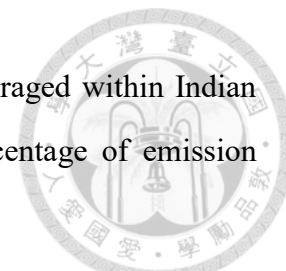
- 
- Atmospheres and Oceans*, 47(1-3), 15-37. doi:10.1016/j.dynatmoce.2008.09.004
- Wang, B., Wu, R., & Lau, K. (2001). Interannual variability of the Asian summer monsoon: Contrasts between the Indian and the western North Pacific–East Asian monsoons. *Journal of Climate*, 14(20), 4073-4090. doi:10.1175/1520-0442(2001)014<4073:IVOTAS>2.0.CO;2
- Wang, C., Kim, D., Ekman, A. M., Barth, M. C., & Rasch, P. J. (2009). Impact of anthropogenic aerosols on Indian summer monsoon. *Geophysical Research Letters*, 36(21). doi:10.1029/2009GL040114
- Wang, S.-Y., Yoon, J.-H., Gillies, R. R., & Cho, C. (2013). What caused the winter drought in western Nepal during recent years? *Journal of Climate*, 26(21), 8241-8256. doi: 10.1175/JCLI-D-12-00800.1
- Wei, L., Lu, Z., Wang, Y., Liu, X., Wang, W., Wu, C., Zhao, X., Rahimi, S., Xia, W., & Jiang, Y. (2022). Black carbon-climate interactions regulate dust burdens over India revealed during COVID-19. *Nature communications*, 13(1), 1839.
- Wu, M., Liu, X., Yu, H., Wang, H., Shi, Y., Yang, K., Darmenov, A., Wu, C., Wang, Z., & Luo, T. (2020). Understanding processes that control dust spatial distributions with global climate models and satellite observations. *Atmospheric Chemistry and Physics*, 20(22), 13835-13855.
- Yang, Y., Ren, L., Wu, M., Wang, H., Song, F., Leung, L. R., Hao, X., Li, J., Chen, L., & Li, H. (2022). Abrupt emissions reductions during COVID-19 contributed to record summer rainfall in China. *Nature communications*, 13(1), 959.
- Zhang, G. J., and N. A. McFarlane, Sensitivity of climate simulations to the parameterization of cumulus convection in the Canadian Climate Centre general circulation model, *Atmosphere-Ocean*, 33, 407–446, 1995.
- Zhou, T., Yu, R., Li, H., & Wang, B. (2008). Ocean forcing to changes in global monsoon precipitation over the recent half-century. *Journal of Climate*, 21(15), 3833-3852. doi:10.1175/2008JCLI2067.1



Table 1 Schemes in CESM

Schemes	Options
The rapid radiation method	RRTMG, Iacono et al. 2008
The cloud microphysics mechanism	Morrison and Gettelman, 2008
The cloud macrophysics	Park, 2010
Shallow convection	Park and Bretherton, 2009
The aerosol scheme	MAM3, Liu et al. 2012
Boundary layer	Bretherton, 2009
Land hydrological processes and land-atmosphere interactions	The Community Land Model V.4, Lawrence et al. 2011; Oleson et al. 2010

Table 2 Emission of anthropogenic aerosols (BC, OC, Sulfate) averaged within Indian region (70°-90°E, 5°-35°N) with Year 2000 data and percentage of emission differences.



	BC	OC	Sulfate
Agricultural waste burning emissions ($\text{Mg} \cdot \text{m}^{-2} \cdot \text{month}^{-1}$)	0.37	0.08	0.02
Domestic emissions ($\text{Mg} \cdot \text{m}^{-2} \cdot \text{month}^{-1}$)	20.34	3.13	2.00
Energy emissions ($\text{Mg} \cdot \text{m}^{-2} \cdot \text{month}^{-1}$)	0.25	0.06	0.31
Industry emissions ($\text{Mg} \cdot \text{m}^{-2} \cdot \text{month}^{-1}$)	4.61	1.86	0.81
Transportation emissions ($\text{Mg} \cdot \text{m}^{-2} \cdot \text{month}^{-1}$)	1.24	1.53	1.02
Waste treatment emissions ($\text{Mg} \cdot \text{m}^{-2} \cdot \text{month}^{-1}$)	0.05	0.05	0.01
Ship emissions ($\text{Mg} \cdot \text{m}^{-2} \cdot \text{month}^{-1}$)	0.05	0.05	0.77
Percentage of total anthropogenic emission (%)	70%	21%	8%
Percentage of emission differences Y2000-Y1850 (%)	68%	22%	9%

Table 3 Ensemble-mean AOD, surface temperature, and surface energy fluxes averaged within Indian region (70°-90°E, 5°-35°N) and pre-monsoon season for AERO and AERO-CTL.

Variables	AERO	AERO-CTL
Aerosol optical depth	0.27	0.06
Net surface shortwave flux (W m ⁻²)	246	-7.26
Net surface longwave flux (W m ⁻²)	109	-2.01
Latent heat flux (W m ⁻²)	74	-0.04
Sensible heat flux (W m ⁻²)	51	0.12
Surface temperature (°C)	27.2	-0.42

Table 4 Concentration differences of each aerosol species; BC, OC, Sulfate and dust in atmosphere averaged within Indian region (70°-90°E, 5°-35°N) with percentage of differences.

	ΔBC ($\mu\text{g}/\text{kg}$)	ΔOC ($\mu\text{g}/\text{kg}$)	$\Delta \text{Sulfate}$ ($\mu\text{g}/\text{kg}$)	ΔDust ($\mu\text{g}/\text{kg}$)
Pre-monsoon	3.75(60%)	1.07(17%)	0.43(7%)	0.98(16%)
Developed monsoon	3.19(73%)	0.87(20%)	0.35(8%)	-0.02(negligibly)
Withdrawal Phase-1	4.22(71%)	1.22(21%)	0.48(8%)	0.02 (negligibly)
Withdrawal Phase+1	4.42(72%)	1.24(20%)	0.50(8%)	-0.01(negligibly)

Table 5 AOD differences of dust and anthropogenic (Anthro) aerosols averaged within Indian region (70°-90°E, 5°-35°N) and northern India (70°-90°E; 20°-35°N) with percentage of differences.

	Δ Dust	Δ Anthro	Δ Dust (Northern)	Δ Anthro (Northern)
Pre-monsoon	0.018(26%)	0.050(74%)	0.027(32%)	0.058(68%)
Developed monsoon	-0.003(-3%)	0.075(103%)	-0.004(-4%)	0.126(104%)
Withdrawal Phase-1	0.004(6%)	0.058(94%)	0.058(8%)	0.086(92%)
Withdrawal Phase+1	-0.005(-9%)	0.068(109%)	-0.011(-10%)	0.119(110%)

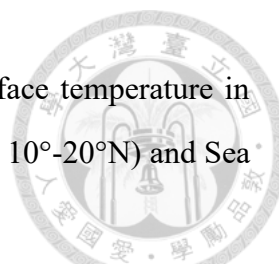


Table 6 Ensemble mean 850hPa atmospheric temperature and surface temperature in AERO, and temperature differences between Land(70°-90°E, 10°-20°N) and Sea (70°-90°E, 0°-10°N).

		850hPa Tair (°C)	850hPa ΔTair	Gradient	Surface T (°C)	Surface ΔT
		AERO	(AERO – CTL)	(Land – Sea)	AERO	(AERO – CTL)
Pre- monsoon	Land	25.3	2.3	2.7	27.1	-0.32
	Sea	22.6	0.4		24.1	0
Developed monsoon	Land	26.2	0.9	0.7	28.2	-0.28
	Sea	25.5	0.3		26.5	0
Withdrawal	Land	25.2	0.7	-0.2	26.6	-0.41
	Sea	25.4	0.3		27.4	0

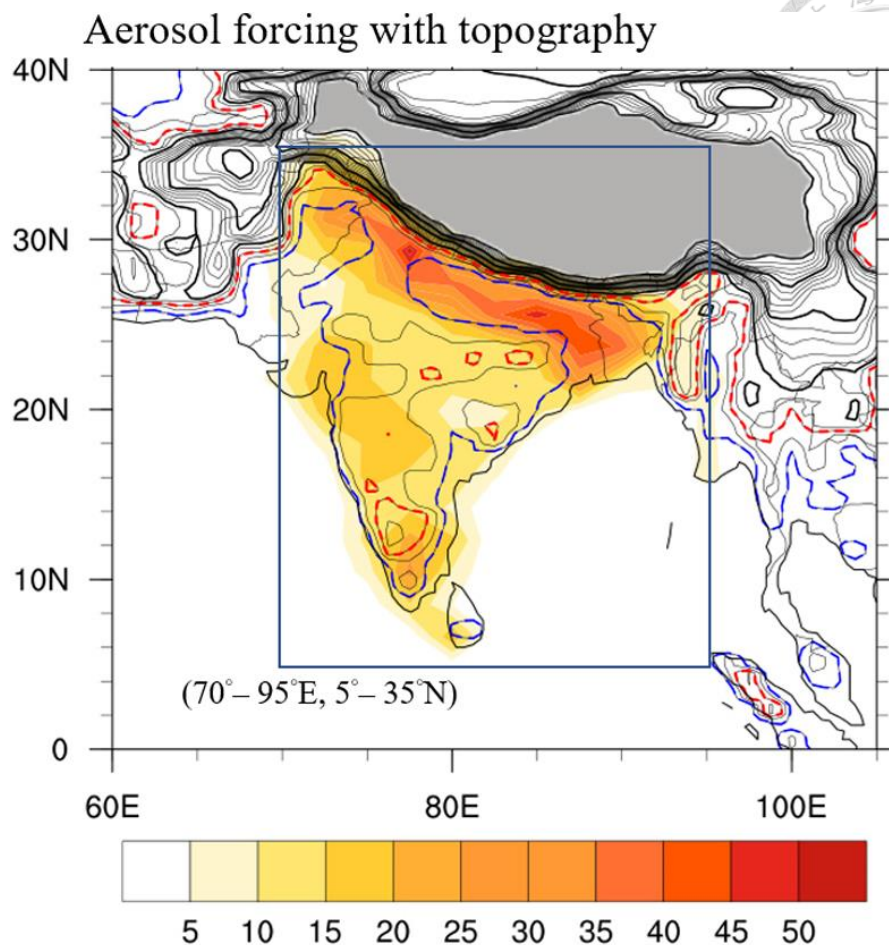


Figure 1 Emission of anthropogenic aerosols (BC, OC, and sulfate) of Year 2000 (shaded, $10^{-1} \cdot \text{Mg} \cdot \text{m}^{-2} \cdot \text{month}^{-1}$) from the IPCC AR5 emission data set (Lamarque et al. 2010a). The sources of emission include industrial, domestic and agriculture activities. Surface topography is superimposed in contour at 200m interval and selected contours highlighted as following: 200m (blue dash), 600m (red dash), 1000m, 2000m, 3000m and 4000m (thick solid). The Tibetan Plateau is denoted by areas with elevation above 4000m and shaded grey.

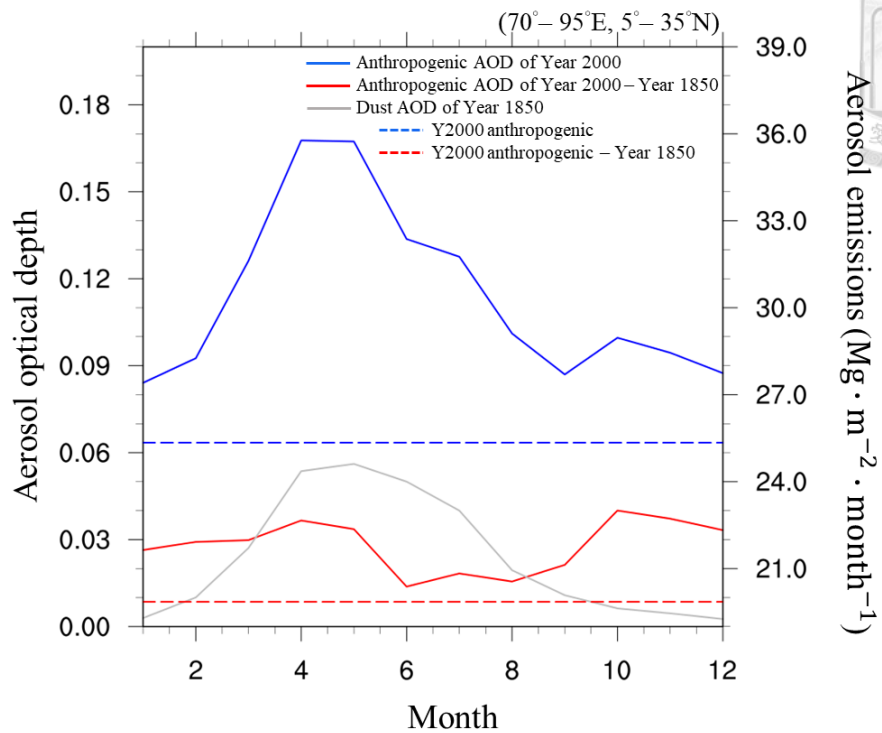


Figure 2 Time series of mean anthropogenic aerosols (BC, OC, sulfate) emission ($\text{Mg} \cdot \text{m}^{-2} \cdot \text{month}^{-1}$) of Year 2000 (*blue dash*), and the simulated annual cycle of anthropogenic aerosol optical depth (AOD, *blue solid*) in the Indian sub-continent region, and the differences of aerosol emission (*red dash*) and AOD (*red solid*) between Year 2000 and Year 1850, and dust AOD (*grey line*) of Year 1850.

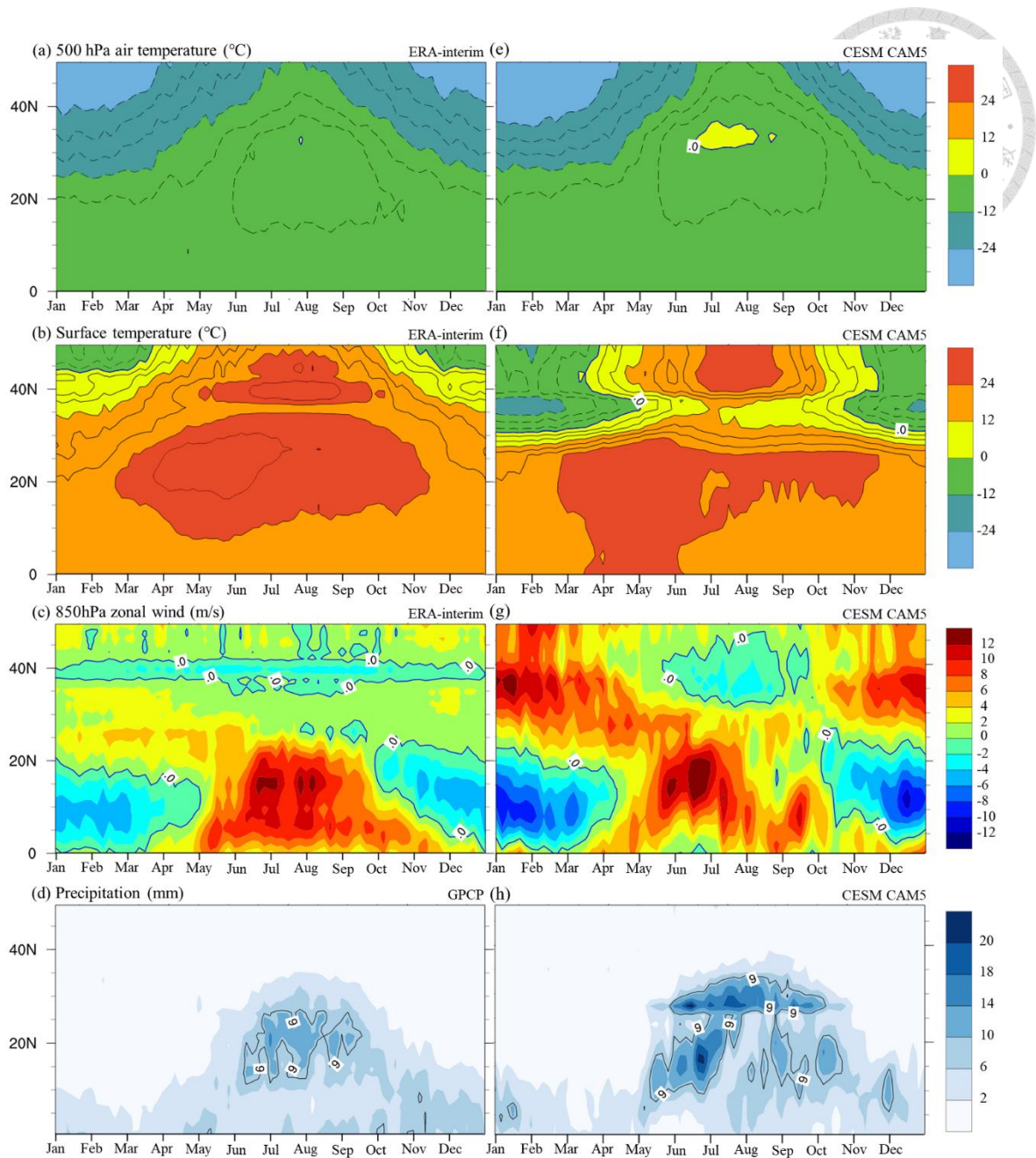


Figure 3 Time-latitude distribution of climatological fields over India longitude sector (70°-90°E) (a) 500 hPa temperature, (b) surface air temperature, (c) 850 hPa zonal wind, and (d) precipitation, derived from ERA-interim and GPCP for 1979-2020. The model simulated climatological fields for the corresponding fields are shown in (e, f, g, h) derived from 25 years of AERO outputs.

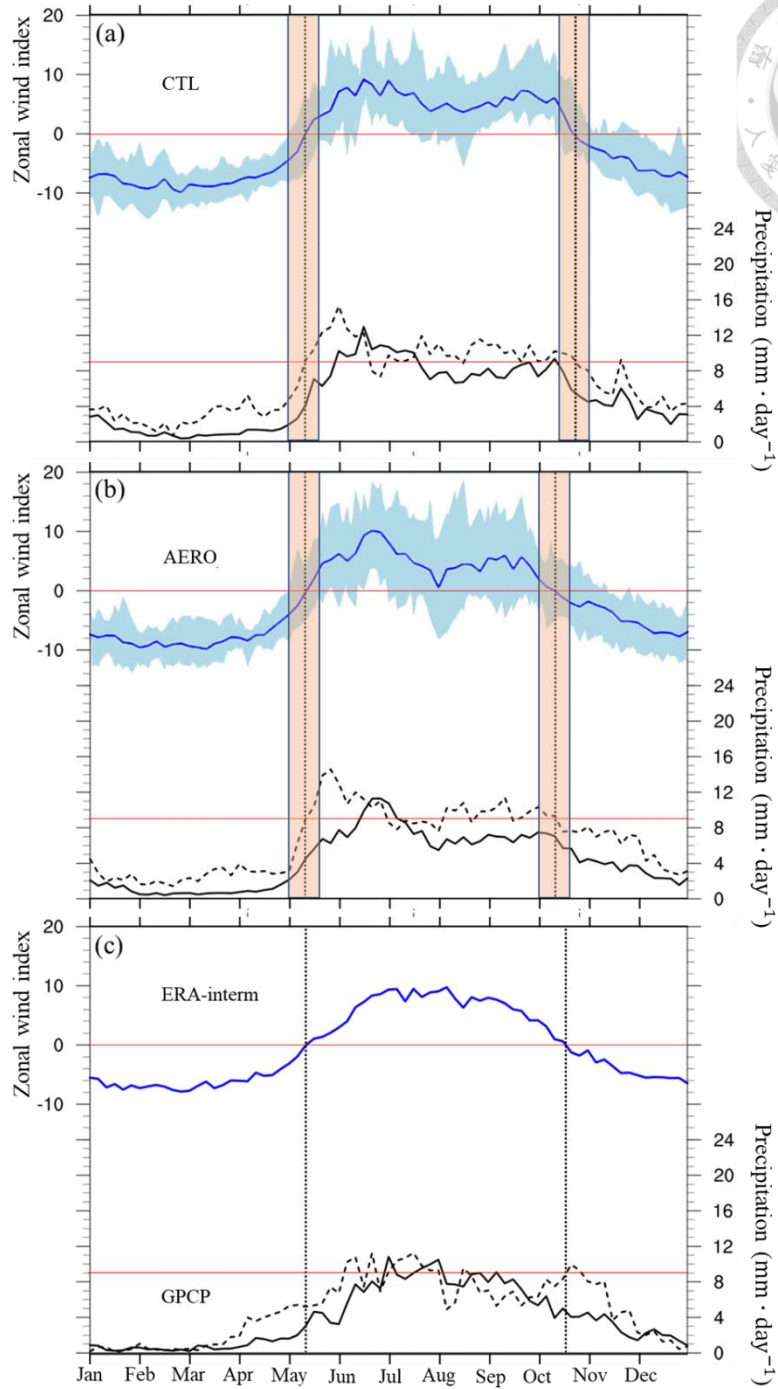

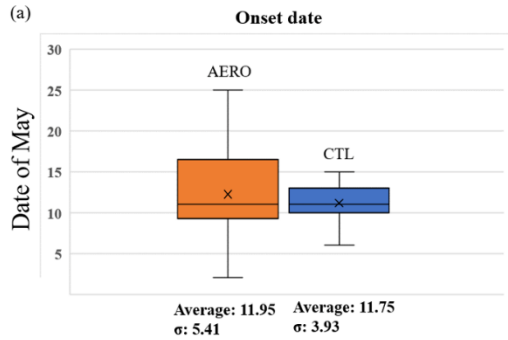


Figure 4 Climatological evolution of the zonal wind index as defined in Wang et al. (2001) (blue line), all-India precipitation (mm, solid line), and Kerala precipitation (mm, dash line, used by India Meteorological Department to define monsoon onset) for (a) CTL, (b) AERO and (c) ERA-interim/GPCP. The standard deviation of the simulated zonal wind



index of the 25 years simulations from CTL and AERO are shown in (a) (b) by blue shadings. The 25-year mean zonal wind index changes sign from negative to positive on May 12 in both CTL and AERO (monsoon onset), and from positive to negative on Oct. 20 in CTL and Oct. 10 in AERO (monsoon withdrawal). The onset and withdrawal dates are marked by vertical dashed lines, and the transition periods are shaded orange within 2 pentads before and after the mean monsoon onset and withdrawal dates. Total monsoon precipitation is 571 mm in CTL and 539 mm in AERO.

Frequency distributions of onset/withdrawal date



Frequency distributions of onset/withdrawal change rate

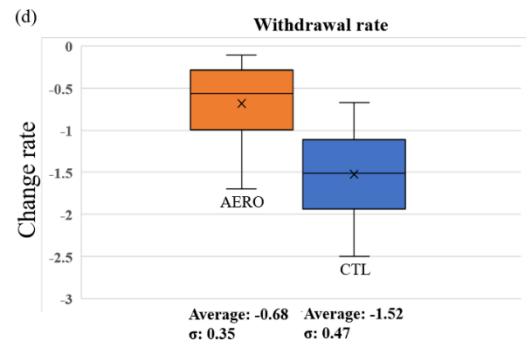
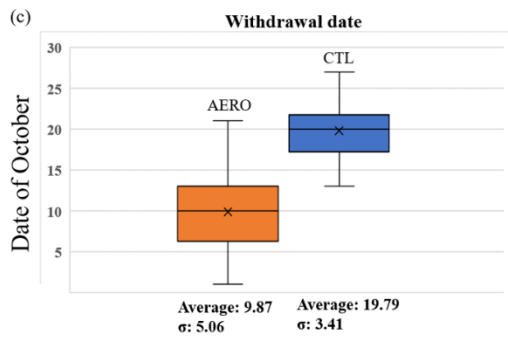
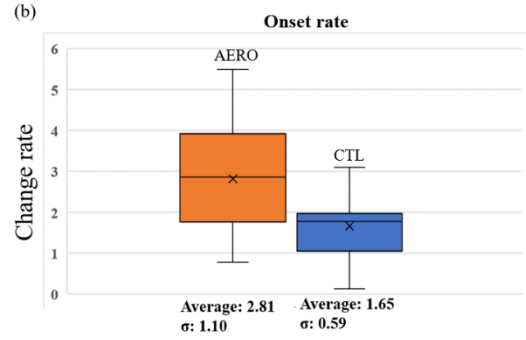


Figure 5 Frequency distributions of India monsoon onset and withdrawal dates (a, c) and their corresponding rate of changes (b, d) of the 25 ensemble years in CTL and AERO.

The statistics is shown in box plots drawn from the first quartile (bottom) to the third quartile (top) and a horizontal line through the box at the median with the mean value marked by a cross and the date of 90% and 10% ranking marked by the sign “—” linked to the box by vertical lines.

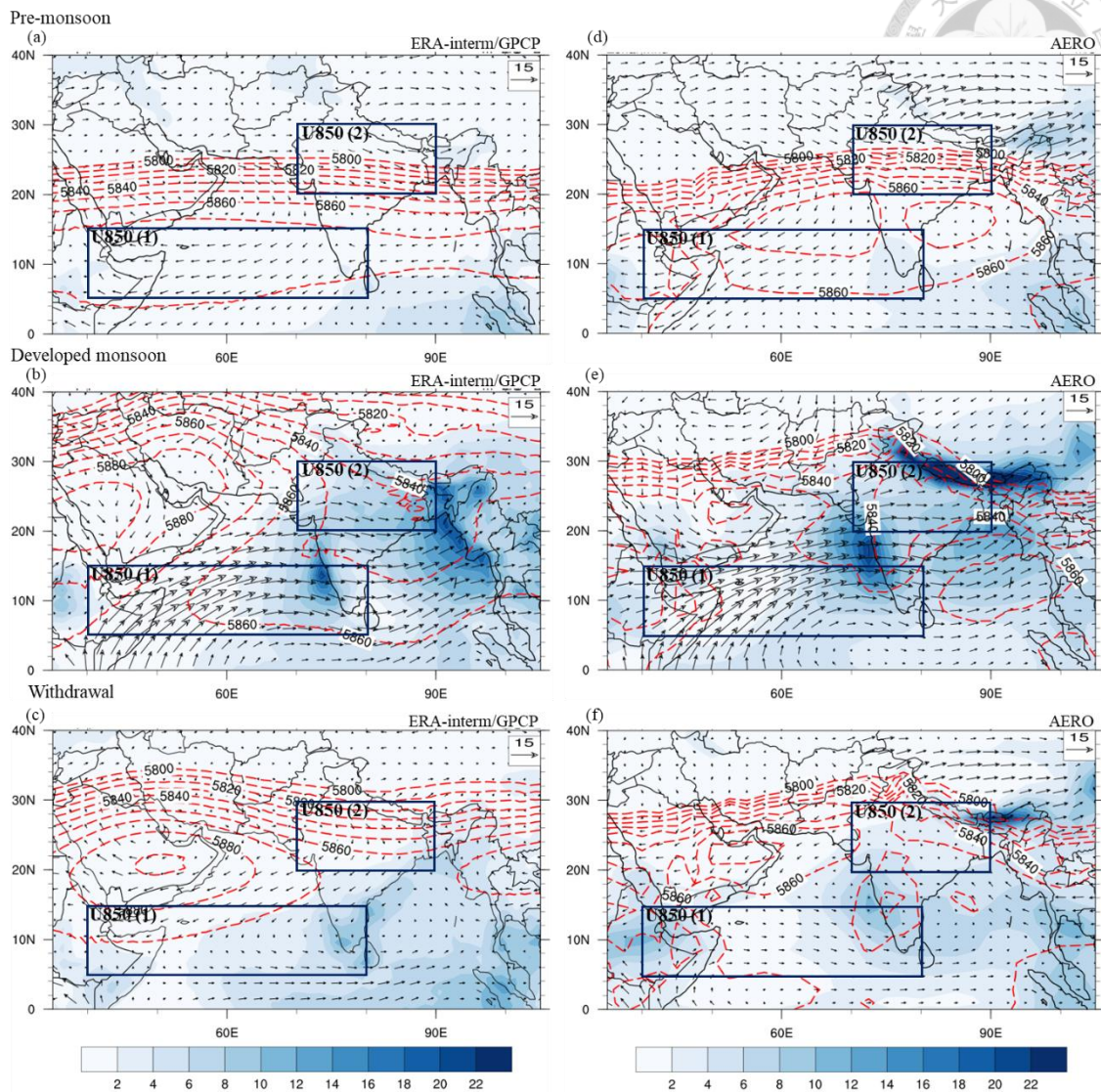


Figure 6 Observed climatological fields of precipitation (mm day^{-1} , shaded), horizontal winds at 850 hPa ($\text{m} \cdot \text{s}^{-1}$, vector) and geopotential height at 500 hPa (m, red dash) in (a) pre-monsoon, (b) post-monsoon, and (c) withdrawal, derived from GPCP and ERA-interim. The simulated ensemble mean fields of 25 years of AERO corresponding to (a, b, c) are shown in (d, e, f). The two rectangles enclosing the area (40° - 80° E, 5° - 15° N) and (70° - 90° E, 20° - 30° N) are used to define the zonal wind index [U850(1)– U850(2)] for the evolution of ISM.

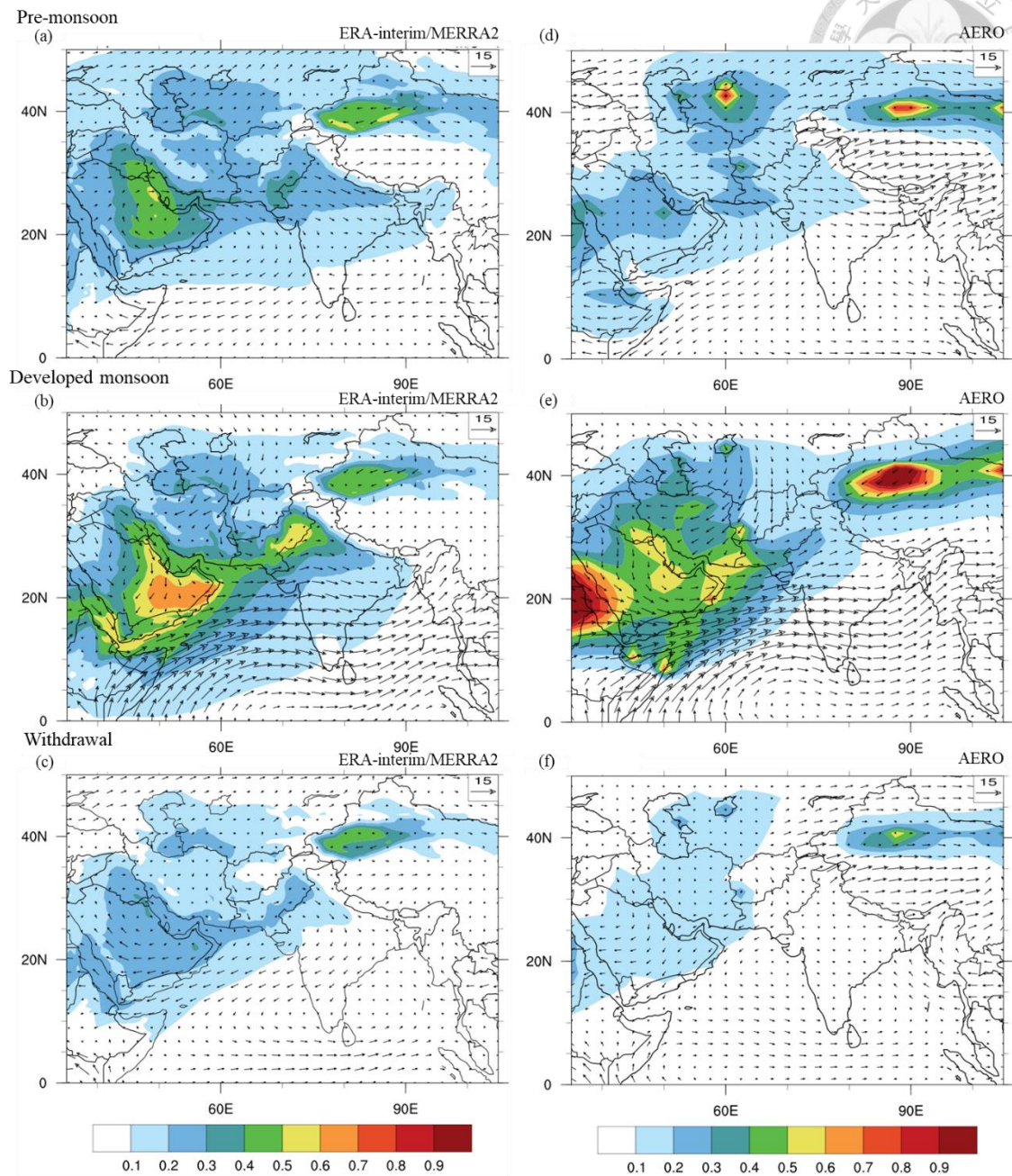


Figure 7 Observed climatological fields of dust AOD (shaded), horizontal winds at 850 hPa ($\text{m} \cdot \text{s}^{-1}$, vector) in (a) pre-monsoon, (b) post-monsoon, and (c) withdrawal, derived from MERRA2 and ERA-interim. The simulated ensemble mean fields of 25 years of AERO corresponding to (a, b, c) are shown in (d, e, f).

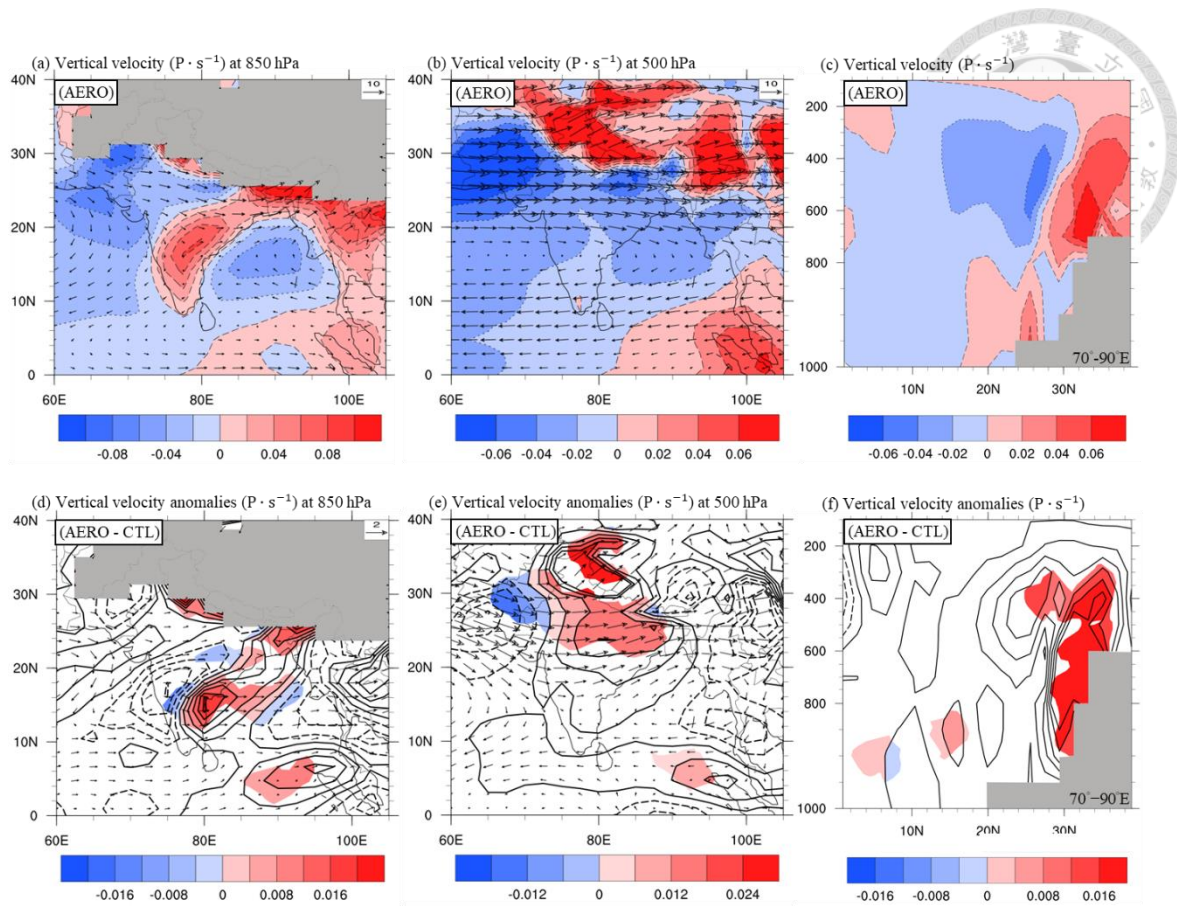


Figure 8 Ensemble mean fields in pre-monsoon period of AERO (March 1 to April 10)

(a) vertical velocity, $-\omega$ (shaded) and horizontal wind ($\text{m} \cdot \text{s}^{-1}$, vector) at 850 hPa, (b) $-\omega$ and horizontal wind at 500 hPa, (c) 70-90°E averaged $-\omega$, (d, e, f) AERO-CTL differences corresponding to the fields shown in a, b, c. Differences of $-\omega$ are shown by contours ($-\omega < 0$ with dashed line, > 0 with thick solid line) with interval 0.04. A confidence level greater than 90% (shaded) use the Student's t-test.

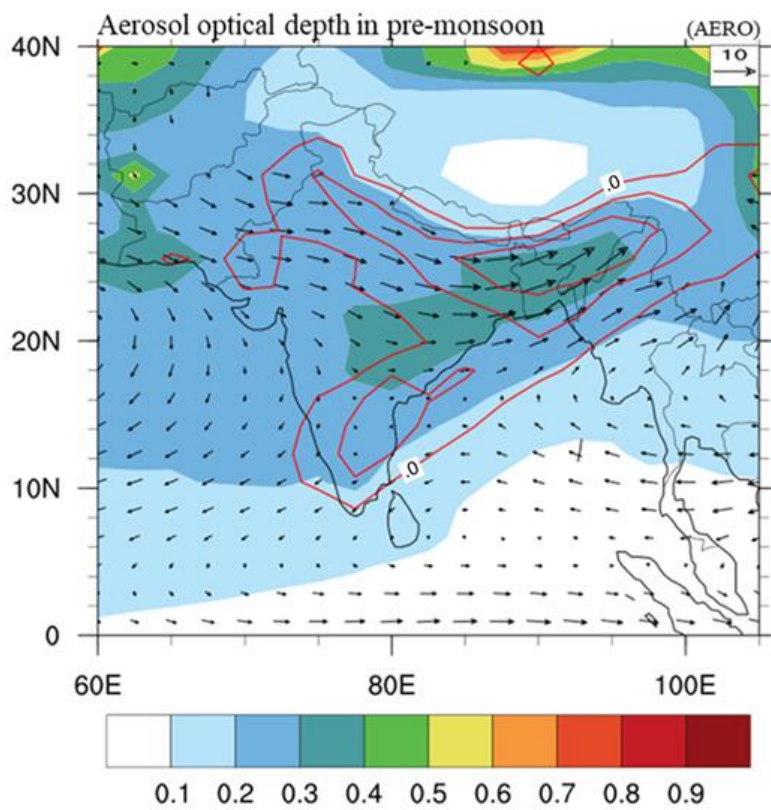


Figure 9 Ensemble mean aerosol optical depth (AOD, *shaded*) and horizontal wind at 850 hPa ($\text{m} \cdot \text{s}^{-1}$, *vector*) in pre-monsoon period of AERO (March 1 to April 10). The AOD differences (AERO – CTL) > 0 are shown by *red contours* with contour interval 0.02 begin from 0.

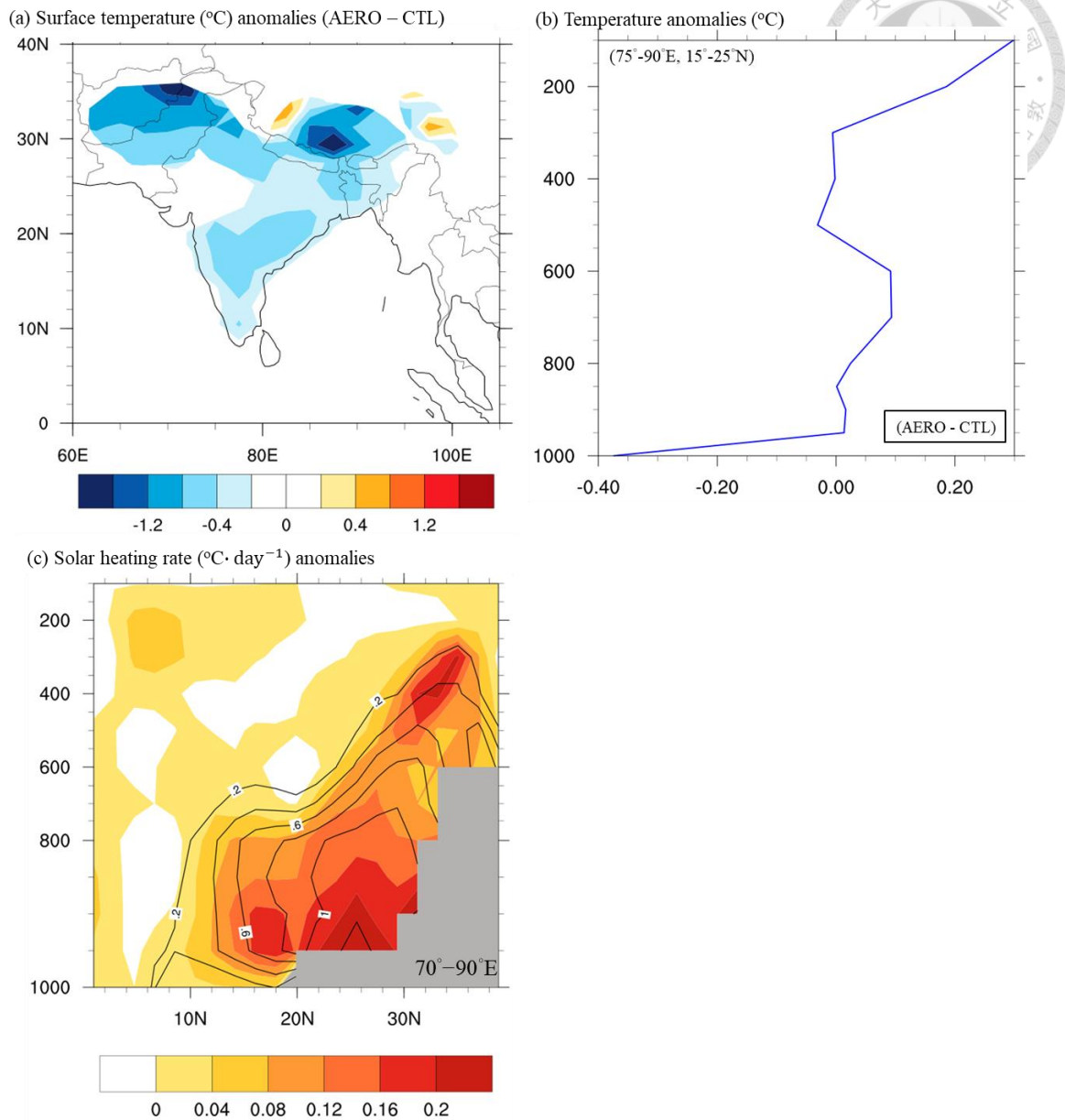


Figure 10 Ensemble mean differences (AERO – CTL) in pre-monsoon period (March 1 to April 10) (a) Surface temperature (°C, *shaded*), (b) The vertical profile of areal mean temperature anomalies (°C) shows in 75°-90°E, 15°-25°N, and (c) Solar heating rate (°C·day⁻¹, *shaded*) and anthropogenic aerosols concentration (mg·m⁻³, *contours at interval 0.2*). A confidence level greater than 90% (*shaded*) use the Student's t-test.

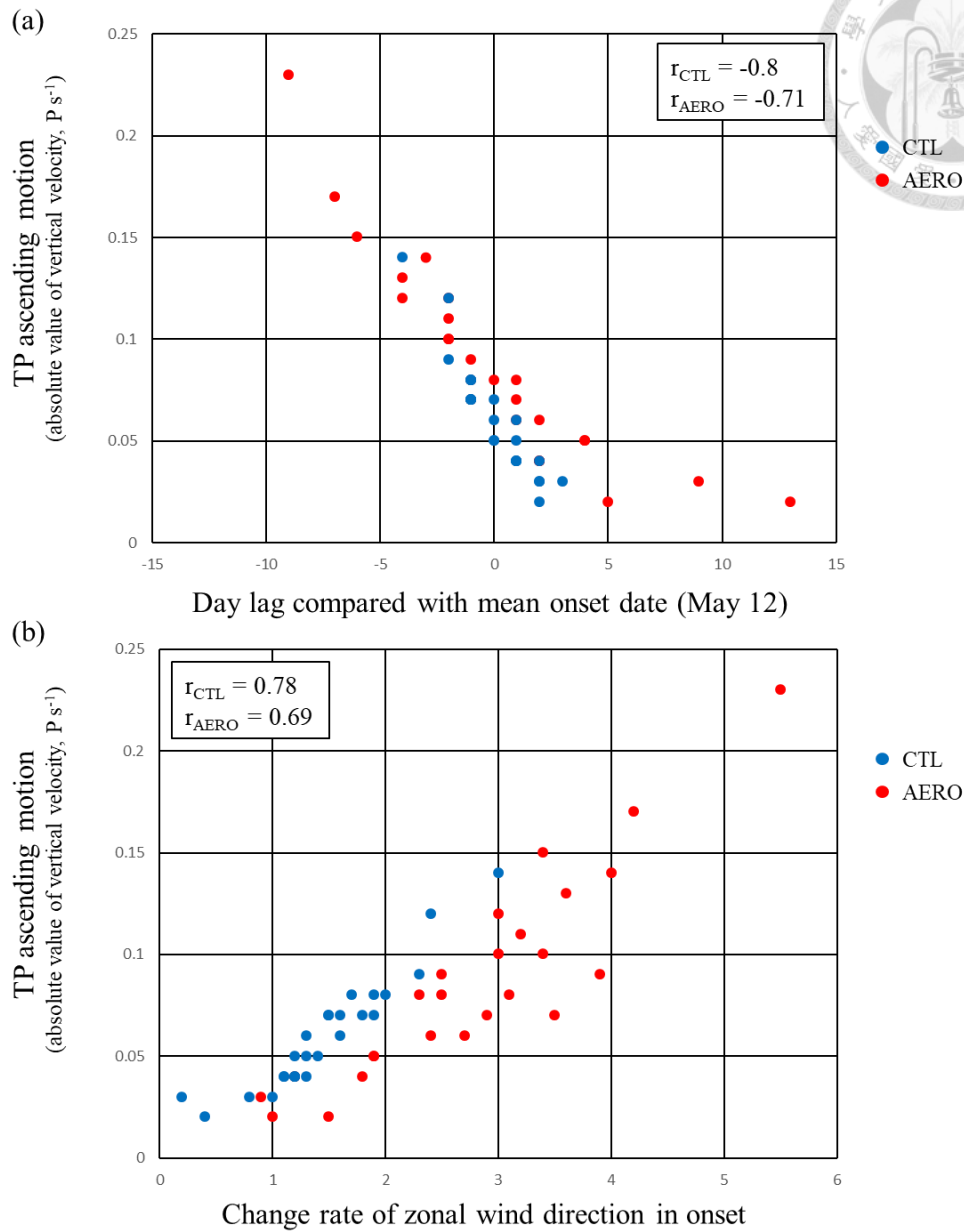
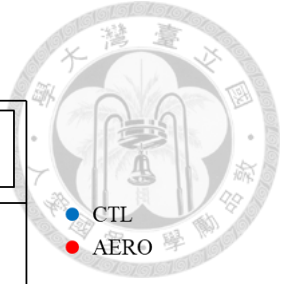


Figure 11 Correlation of 500 hPa TP ascending motion with (a) onset date and (b) ISM change rate over the pre-monsoon season (March 1 to April 10) in AERO (red dots) and CTL (blue dots). The correlation coefficient of TP ascending motion with onset date is -0.71 (-0.8) in AERO (CTL) and with change rate is 0.69 (0.78) in AERO (CTL).

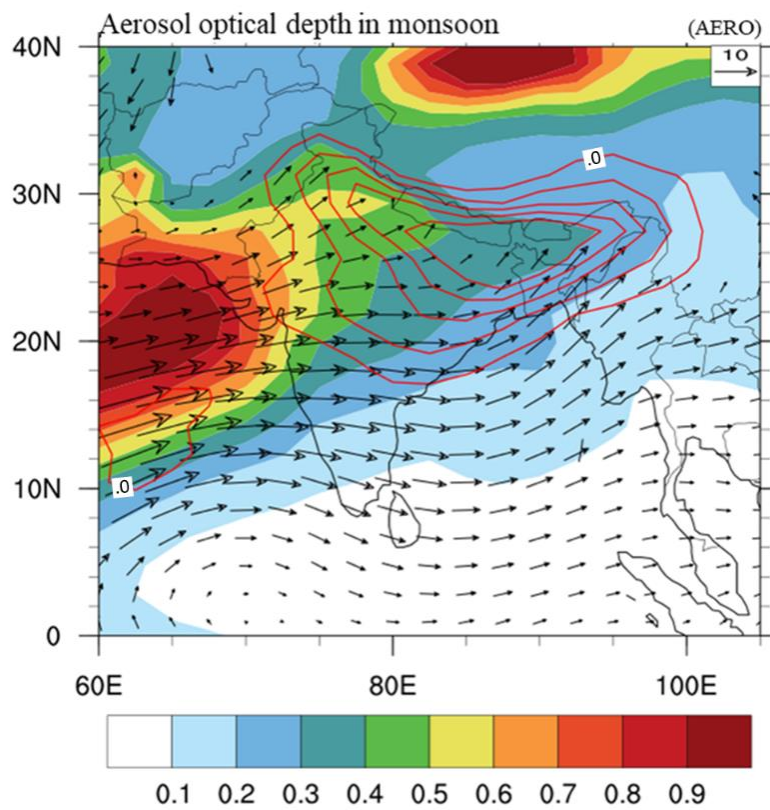


Figure 12 Ensemble mean aerosol optical depth (AOD, *shaded*) and horizontal wind at 850 hPa ($\text{m} \cdot \text{s}^{-1}$, *vector*) in developed monsoon period of AERO (May 26 to August 3). The AOD differences (AERO – CTL) > 0 are shown by *red contours* with contour interval 0.02 begin from 0.

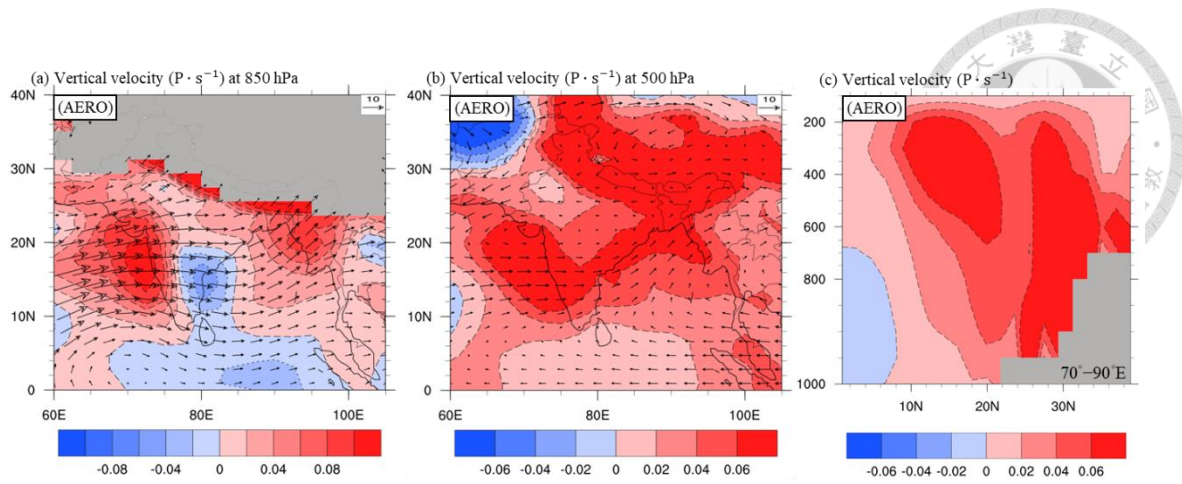


Figure 13 Ensemble mean fields in developed monsoon period of AERO (May 26 to August 3) (a) $-\omega$ (shaded) and horizontal wind ($\text{m} \cdot \text{s}^{-1}$, vector) at 850 hPa, (b) $-\omega$ and horizontal wind at 500 hPa, (c) 70° - 90° E averaged $-\omega$.

Surface temperature (°C) anomalies (AERO – CTL)

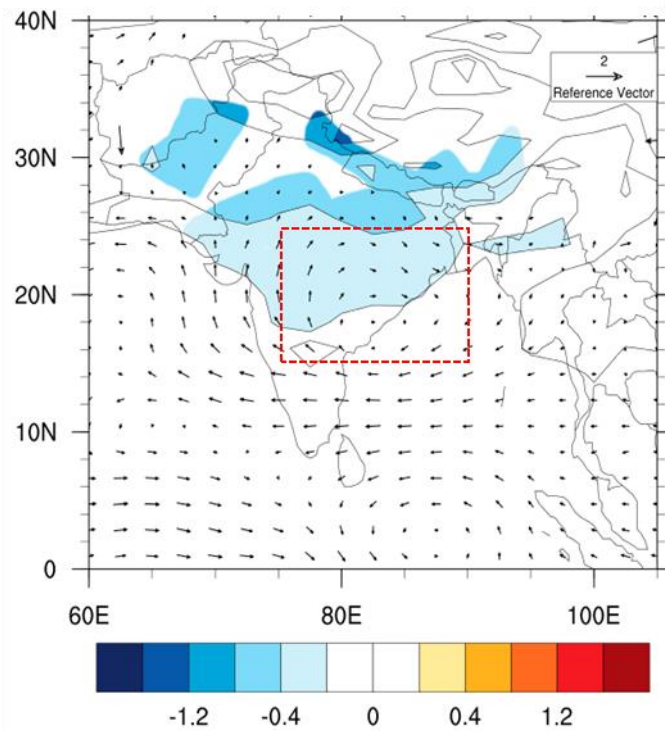


Figure 14 Ensemble mean differences (AERO – CTL) of surface temperature (°C, shaded), and 850 hPa circulation ($\text{m}\cdot\text{s}^{-1}$, vector) in developed monsoon period of AERO (May 26 to August 3). A confidence level greater than 90% (shaded) use the Student's t-test.

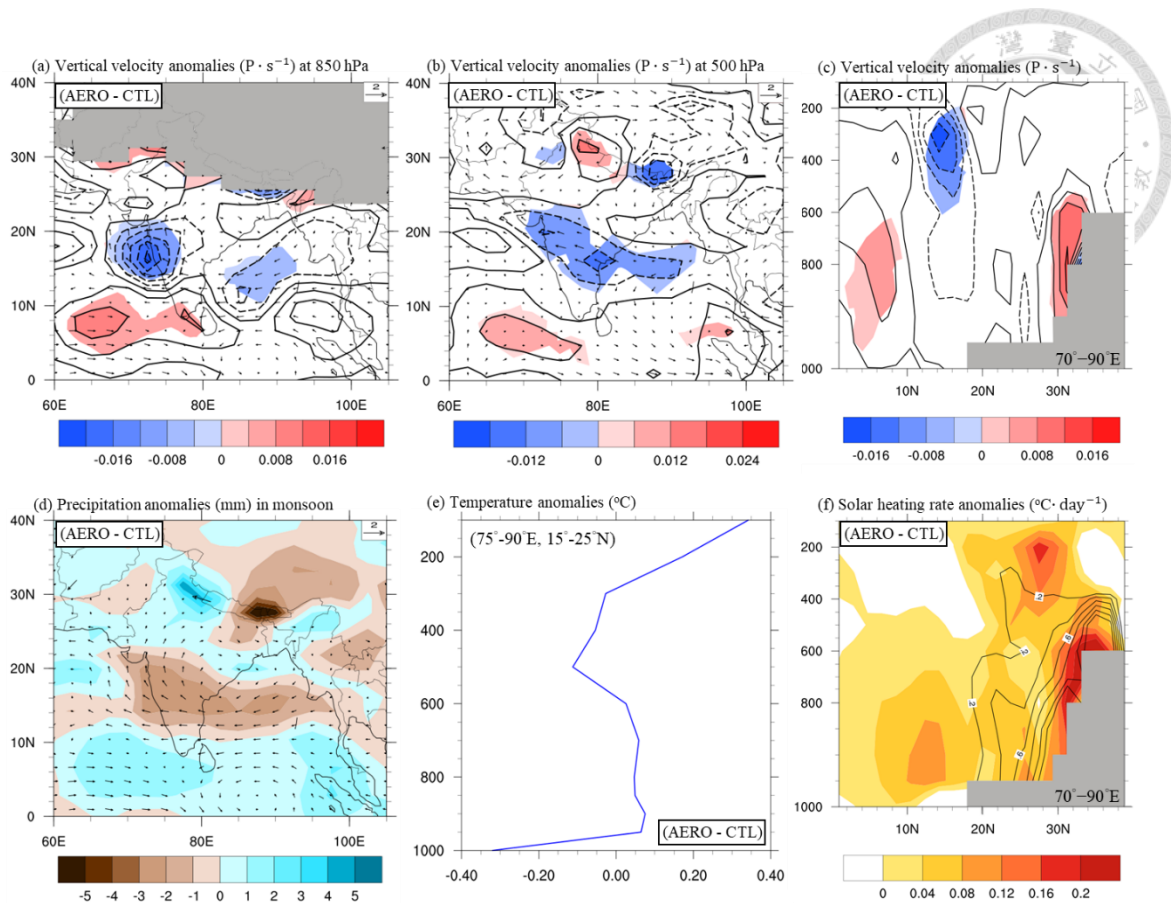


Figure 15 Ensemble mean differences fields (AERO-CTL) during developed monsoon period (May 26 to August 3) of $-\omega$ are shown by contours ($-\omega < 0$ with dashed line, > 0 with thick solid line) with interval 0.04 and horizontal wind ($m \cdot s^{-1}$, vector) at (a) 850 hPa, and (b) 500 hPa, (c) 70° - 90° E averaged $-\omega$. A confidence level greater than 90% (shaded) use the Student's t-test. (d) The differences of precipitation (mm) are shown by shaded with 850-hPa horizontal winds ($m \cdot s^{-1}$, vector). (e) The vertical profile of areal mean temperature anomalies ($^{\circ}$ C) shows in 75° - 90° E, 15° - 25° N, and (f) the solar heating rate anomalies ($^{\circ}$ C day $^{-1}$, shaded) are shown with anthropogenic aerosols concentration anomalies ($mg \cdot m^{-3}$, contour); each contour is $0.2 \text{ mg} \cdot m^{-3}$.

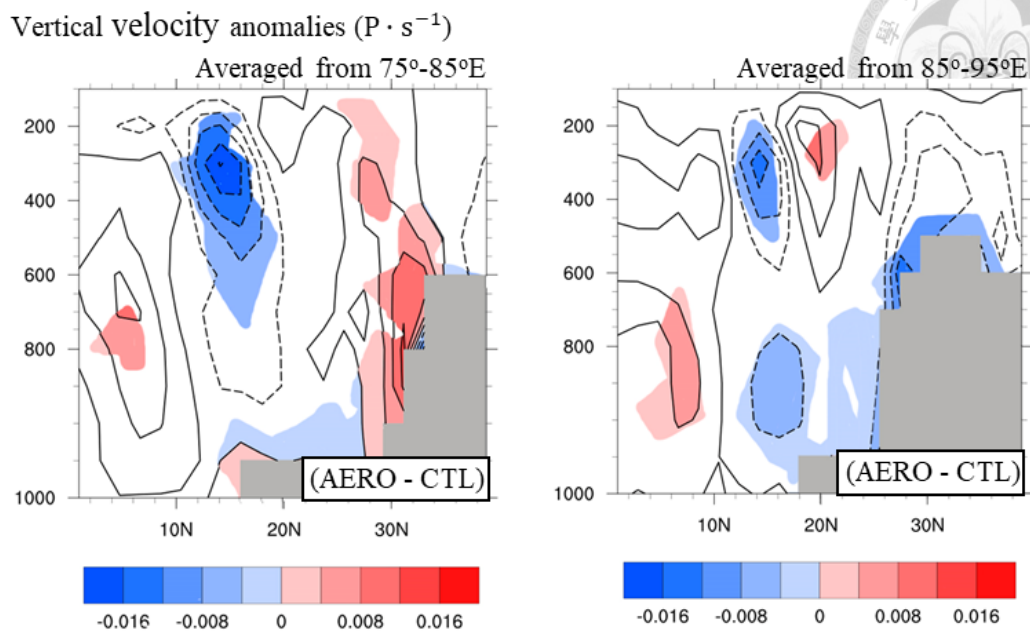


Figure 16 Ensemble mean differences fields (AERO-CTL) during developed monsoon period (May 26 to August 3) of $-\omega$ are shown by contours ($-\omega < 0$ with dashed line, > 0 with thick solid line) with interval 0.04 in 75° - 85° E and 85° - 95° E averaged $-\omega$. A confidence level greater than 90% (shaded) use the Student's t-test.

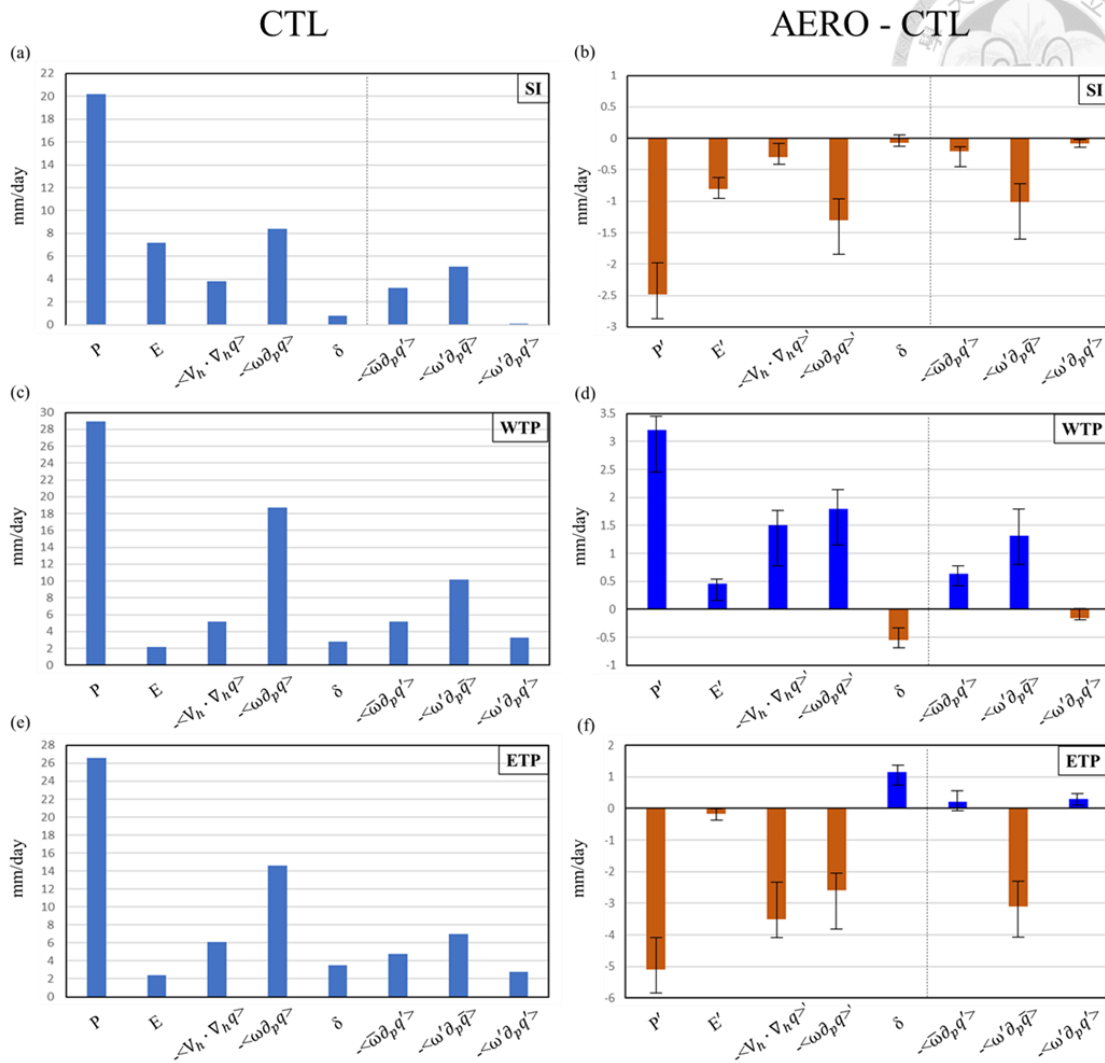


Figure 17 Ensemble mean in AERO and differences for moisture budget components averaged over the SI(10°-20°N, 70°-90°E), WTP(25°-35°N, 75°-85°E), ETP(25°-35°N, 85°-95°E). P is precipitation; E is evaporation; $-\langle V_h \cdot \nabla_h q \rangle$ is the horizontal moisture advection; $-\langle \omega \partial_p q \rangle$ is the vertical moisture advection; δ is the residual term; $-\langle \bar{\omega} \partial_p q' \rangle$, $-\langle \omega' \partial_p \bar{q} \rangle$ and $-\langle \omega' \partial_p q' \rangle$ are the dynamic, thermodynamic, and nonlinear components of vertical moisture advection term, respectively. The terms with ' means difference.

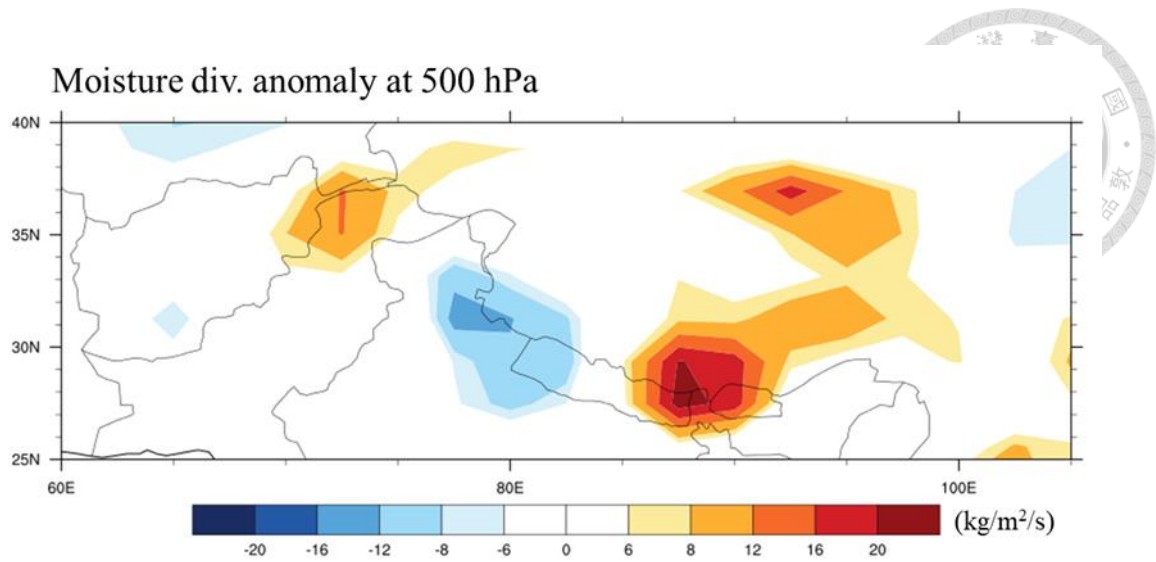


Figure 18 Ensemble mean differences of moisture divergence ($\text{kg/m}^2/\text{s}$) at 500 hPa in developed monsoon period (May 26 to August 3) over the Southern edge of TP.

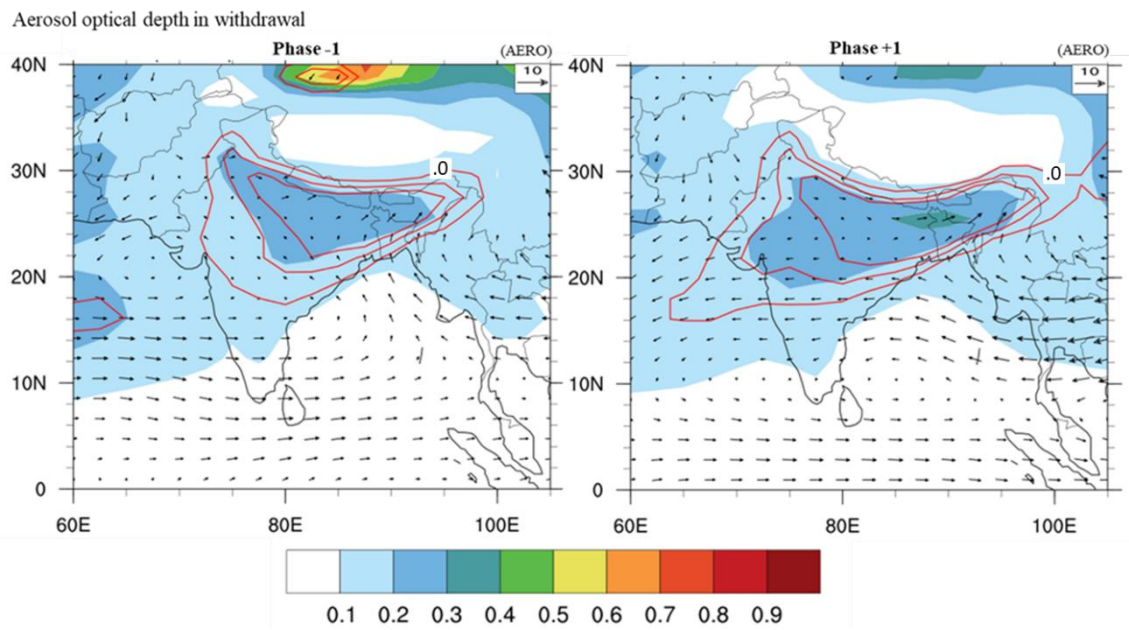


Figure 19 Aerosol optical depth (AOD, *shaded*) and 850 hPa horizontal circulation ($\text{m} \cdot \text{s}^{-1}$, *vector*) in withdrawal period (September 23 to October 27) of AERO. The Phase-1 and the Phase+1 represent the two weeks before and after the withdrawal date of ensemble-mean fields. *Red contour* means AOD anomalies (AERO – CTL) > 0, each contour is 0.02.

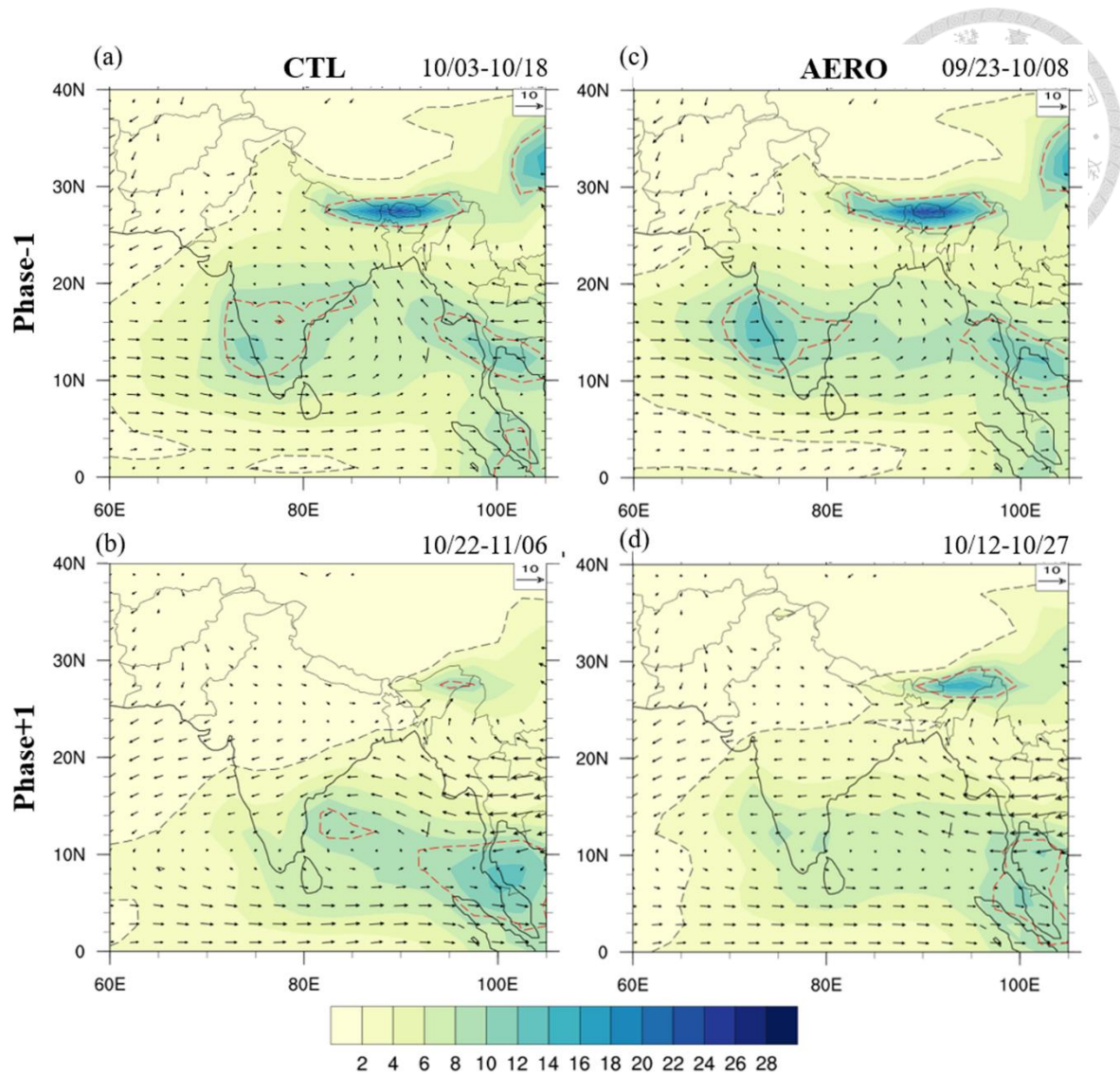


Figure 20 Precipitation (mm, *shaded*) and 850-hPa horizontal winds ($\text{m} \cdot \text{s}^{-1}$, *vector*) averaged in (a) CTL Phase-1 (Oct. 3 to Oct. 18), (b) CTL Phase+1 (Oct. 22 to Nov. 6), (c) AERO Phase-1 (Sep. 23 to Oct. 8), and (d) AERO Phase+1 (Oct. 12 to Oct. 27). *Black dash line* equals to 2 mm, and *red dash line* equals to 9 mm.

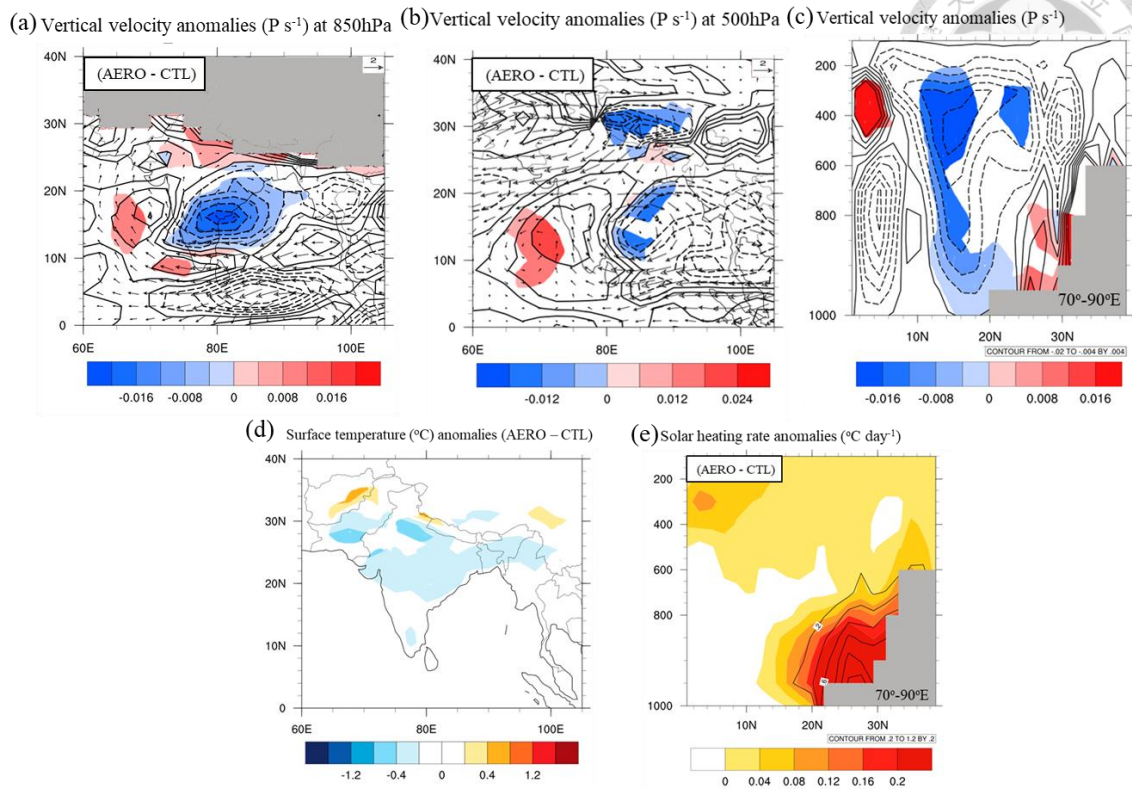


Figure 21 Ensemble mean differences fields (AERO-CTL) during withdrawal period (September 23 to November 6) of $-\omega$ are shown by contours ($-\omega < 0$ with dashed line, > 0 with thick solid line) with interval 0.04 and horizontal wind ($m s^{-1}$, *vector*) at (a) 850 hPa, and (b) 500 hPa, (c) 70°-90°E averaged $-\omega$. A confidence level greater than 90% (shaded) use the Student's t-test. (d) The differences of surface temperature ($^{\circ}C$), and (e) the solar heating rate anomalies ($^{\circ}C day^{-1}$, shaded) are shown with anthropogenic aerosols concentration anomalies ($mg \cdot m^{-3}$, *contour*); each contour is $0.2 mg \cdot m^{-3}$.

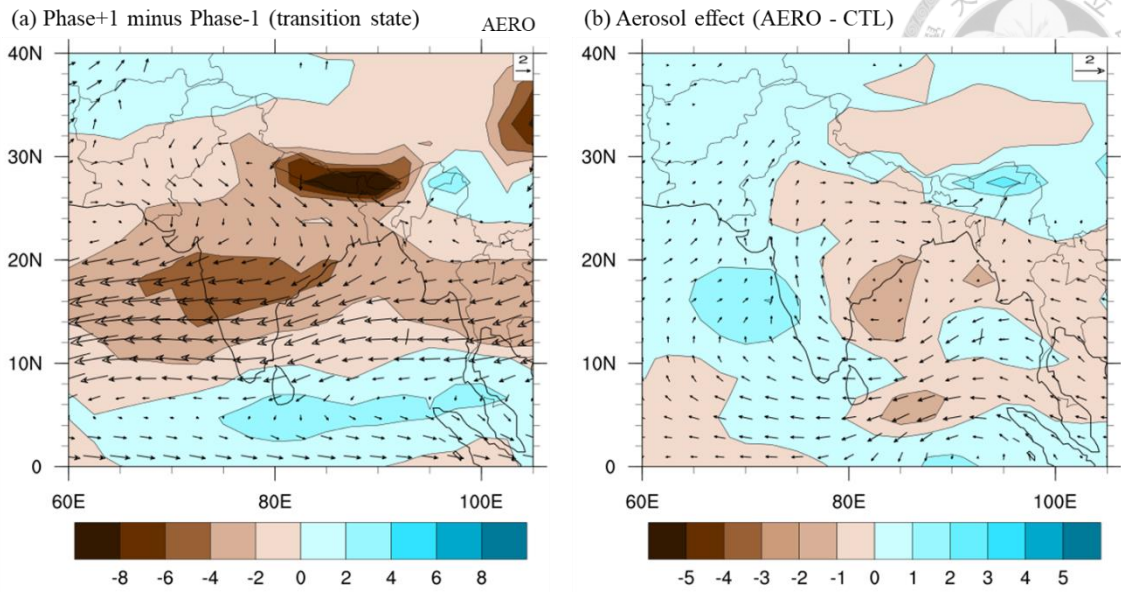


Figure 22 Difference fields of precipitation (mm, shaded) and 850-hPa horizontal winds for (a) Phase+1 minus Phase-1 in AERO, and (b) withdrawal (Phase-1 to Phase+1) differences (AERO minus CTL).

Δ AOD of dust with Δ UV850

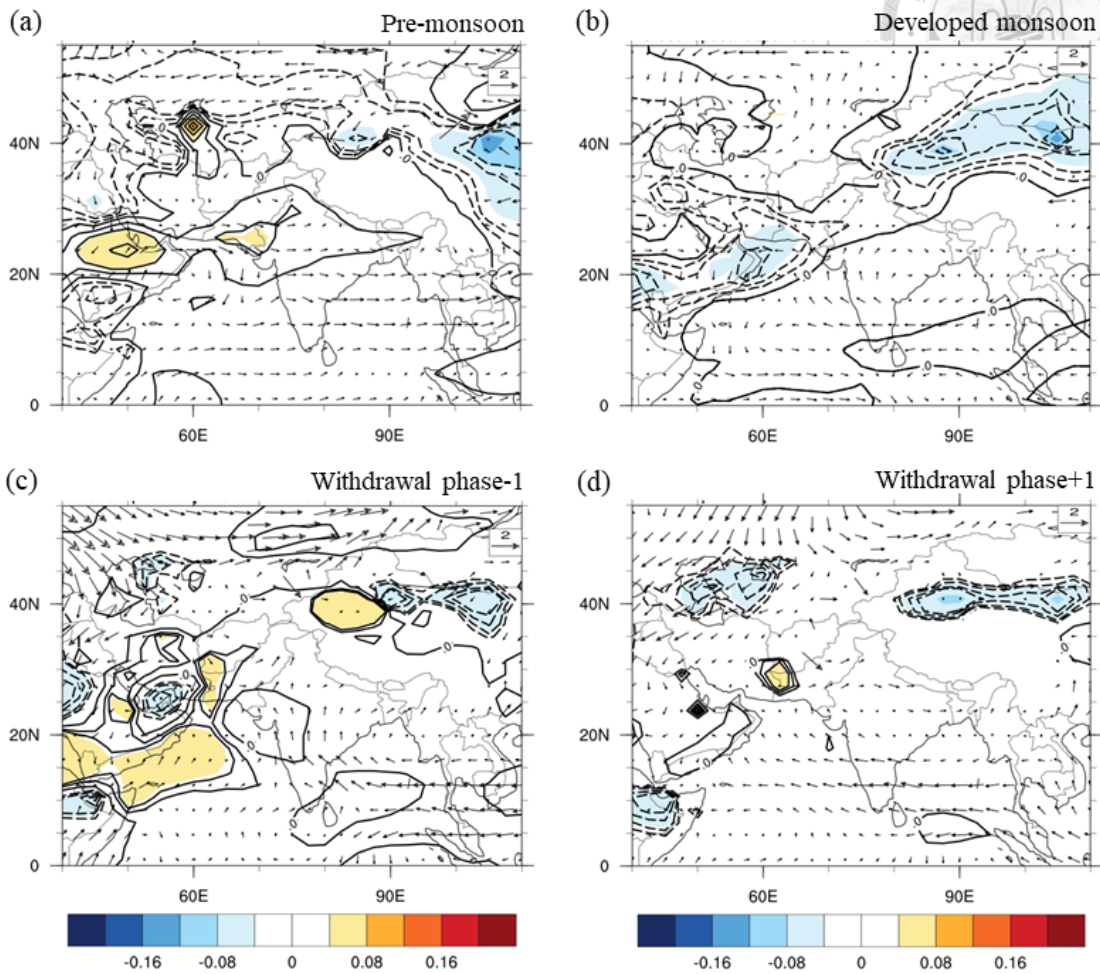


Figure 23 Differences of dust AOD (*contour*, $\Delta < 0$ with dashed line, $\Delta > 0$ with thick solid line) and 850-hPa horizontal winds ($\text{m} \cdot \text{s}^{-1}$, *vector*) averaged in (a) pre-monsoon (March 1 to April 10), (b) developed monsoon (May 26 to August 3), (c) withdrawal Phase-1 (Sep. 23 to Oct. 8), and (d) AERO Phase+1 (Oct. 12 to Oct. 27). The Contour plot with interval 0.02, and significant Δ AOD with a confidence level greater than 90% using the Student's t-test.

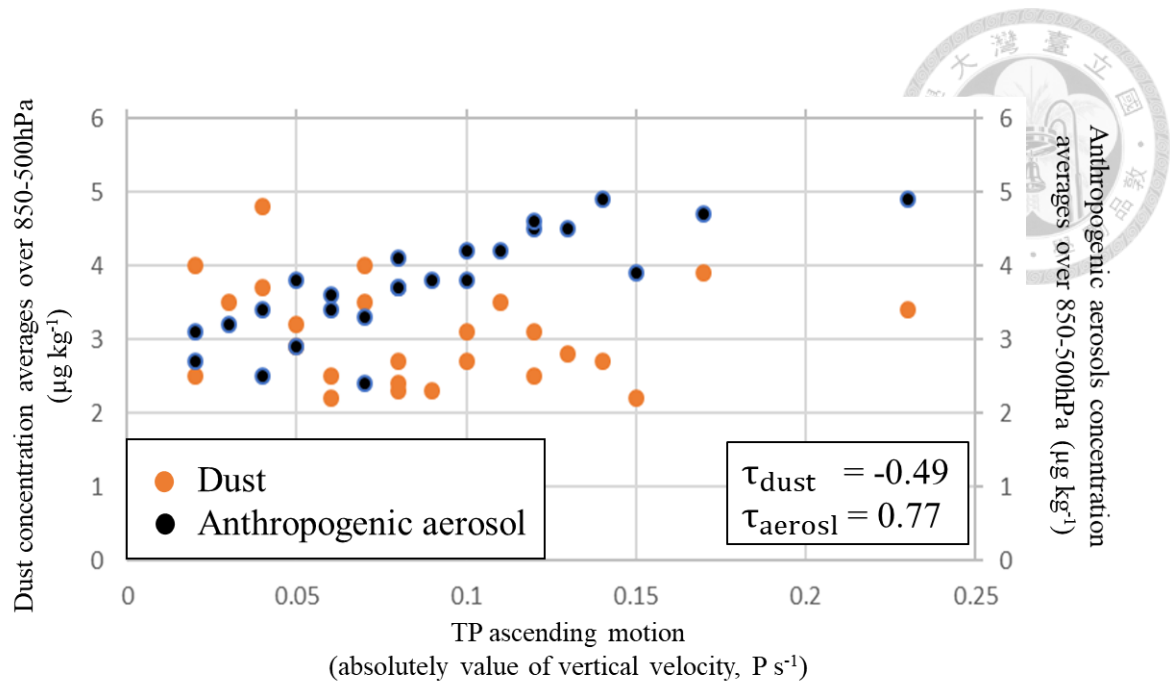


Figure 24 Correlation of 500 hPa TP ascending motion with 850-500hPa Northern Indian (25°-35°N, 70°-90°E) averaged dust (orange dots) and anthropogenic aerosol (black dots) concentration over the pre-monsoon season (March 1 to April 10) in AERO. The correlation coefficient of TP ascending motion with dust is -0.49 and anthropogenic aerosol is 0.77 in AERO.